

PAPER

# Interpretable High-order Knowledge Graph Neural Network for Predicting Synthetic Lethality in Human Cancers

Xuexin Chen,<sup>1</sup> Ruichu Cai,<sup>1,2,\*</sup> Zhengting Huang,<sup>1</sup> Zijian Li,<sup>3</sup> Jie Zheng<sup>4,5</sup>  
and Min Wu<sup>6,\*</sup>

<sup>1</sup>School of Computer Science, Guangdong University of Technology, 510006, Guangdong, China, <sup>2</sup>Pazhou Laboratory (Huangpu), Guangzhou, China, <sup>3</sup>Mohamed bin Zayed University of Artificial Intelligence, Abu Dhabi, <sup>4</sup>School of Information Science and Technology, ShanghaiTech University, 201210, China, <sup>5</sup>Shanghai Engineering Research Center of Intelligent Vision and Imaging, ShanghaiTech University, 201210, China and <sup>6</sup>Institute for Infocomm Research (I<sup>2</sup>R), A\*STAR, 138632, Singapore

\*Corresponding authors: cairuichu@gmail.com, wumin@i2r.a-star.edu.sg

FOR PUBLISHER ONLY Received on Date Month Year; revised on Date Month Year; accepted on Date Month Year

## Abstract

Synthetic lethality (SL) is a promising gene interaction for cancer therapy. Recent SL prediction methods integrate knowledge graphs (KGs) into graph neural networks (GNNs) and employ attention mechanisms to extract local subgraphs as explanations for target gene pairs. However, attention mechanisms often lack fidelity, typically generate a single explanation per gene pair, and fail to ensure trustworthy high-order structures in their explanations. To overcome these limitations, we propose Diverse Graph Information Bottleneck for Synthetic Lethality (DGIB4SL), a KG-based GNN that generates multiple faithful explanations for the same gene pair and effectively encodes high-order structures. Specifically, we introduce a novel DGIB objective, integrating a Determinant Point Process (DPP) constraint into the standard IB objective, and employ 13 motif-based adjacency matrices to capture high-order structures in gene representations. Experimental results show that DGIB4SL outperforms state-of-the-art baselines and provides multiple explanations for SL prediction, revealing diverse biological mechanisms underlying SL inference.

**Key words:** synthetic lethality, machine learning explainability, graph neural network, information bottleneck

## Introduction

Synthetic Lethality (SL) is a promising type of genetic interaction where the co-occurrence of two (or more) genetic events leads to cell death, while the occurrence of either event is compatible with cell viability. SL has become a cornerstone of anti-cancer drug research, by targeting a gene that is nonessential in normal cells but synthetic lethal with a gene with cancer-specific alterations, which would enable the selective killing of cancer cells without harming normal cells. For example, AZD1775, a WEE1 Inhibitor, is based on the SL interaction between WEE1 and p53 mutations [2]. Despite extensive research on SL through high-throughput wet-lab screening methods, these methods often face various challenges, such as high costs and inconsistencies across platforms. Thus, predicting SL using computational models becomes highly complementary to wet-lab approaches.

SL prediction approaches can be broadly categorized into statistical inference methods, network-based methods, and supervised machine learning methods. Among these, graph neural networks (GNNs) are currently the most popular model, largely owing to their ability to model complex gene

interactions [3]. Although many SL gene pairs have been identified, few of them have been applied to cancer treatment, as understanding the underlying biological mechanisms remains a critical challenge. Unfortunately, most GNNs lack the capability to explain SL mechanisms. To address this, methods incorporating attention mechanisms and knowledge graphs (KGs, a heterogeneous graph containing biological entities and their relationships) have emerged [3, 4, 5, 6]. These approaches enable the identification of crucial edges or semantic features in KGs while predicting SL interaction.

Although KG-based methods with attention mechanisms improve the interpretability of SL predictions, they still face three major challenges. First, explanations based on the attention mechanisms often lack reliability, since they tend to assign higher weights to frequent edges and produce unstable explanations across independent runs of the same model [7, 8, 9, 10, 11]. As illustrated by the examples in Fig. 1, the gray subgraph, predicted by attention-based methods, includes a red dashed edge labeled “repair”. This edge, irrelevant to the SL mechanism, is assigned higher importance due to its frequent occurrence in the KG. Second, existing KG-based methods generate only a single core subgraph to explain predictions for

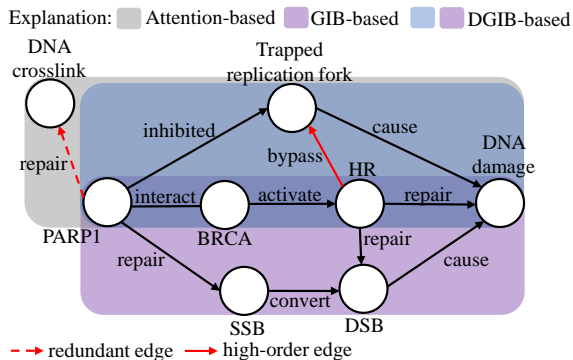


**Fig. 1.** Toy example of a knowledge graph with self-loops integrating biological context and relevant mechanisms between the given gene pair BRCA1 and PARP1. The purple and blue subgraphs illustrate mechanisms where either the conversion of SSBs to DSBs or the blockage of replication forks leads to DNA damage in the absence of HR [1]. The gray subgraph represents the predicted core subgraph of an attention-based method. A GIB-based method identifies only one correct subgraph, while our DGIB4SL can find all correct subgraphs (purple and blue). HR, SSB and DSB are abbreviations for “Homologous Recombination”, “Single Strand Break” and “Double Strand Break”, respectively. The self-loops are not depicted for brevity.

a given gene pair, even though multiple subgraphs may provide valid explanations [1]. As illustrated in Fig. 1, the purple subgraph highlights a mechanism where SSB converts to DSB, while the blue subgraph represents replication fork blocking. Both subgraphs explain the SL interaction between PARP1 and BRCA [1]. Third, the high-order structures contained in the explanations generated by KG-based methods are often untrustworthy, since the key step of these self-explainable methods, learning gene representation for prediction, cannot capture the information of the interactions between the neighbors (high-order), although the information between a gene and its neighbors can be effectively captured (low-order). For instance, as shown in Fig. 1, the “DNA damage” node representation produced by KG-based methods remains unchanged, regardless of the high-order edge “HR  $\xrightarrow{\text{bypass}}$  Trapped replication fork”. We thus ask: for a gene pair, how to find multiple rather than one faithful core subgraphs and encode their high-order graph information for prediction?

Our main contribution lies in addressing this question by proposing the Diverse Graph Information Bottleneck for Synthetic Lethality (DGIB4SL), an interpretable GNN model for SL prediction on KGs, hinging on the motif-based GNN encoder and our proposed DGIB objective. First, to alleviate instability and the bias toward frequent edges in attention-based methods, unlike the cross-entropy loss commonly used in attention-based methods, DGIB4SL employs the GIB principle [12], widely applied in interpretable GNNs [13, 14], to define a core subgraph from the neighborhood of a gene pair. GIB provides a principled objective function for graph representation learning, determining which data aspects to preserve and discard [15]. However, the standard GIB objective identifies only a single core subgraph for each gene pair. To capture all relevant core subgraphs from the enclosing graph, such as the purple and blue subgraphs in Fig. 1, we propose the novel Diverse GIB (DGIB) objective function, which incorporates a Determinant Point Process (DPP) [16] constraint into GIB. DPP quantifies diversity by measuring differences between core subgraphs through the determinant of

the inner product of their subgraph representations. Second, to encode both high-order and low-order pair-wise structural information from the candidate core subgraphs for prediction, DGIB4SL employs a motif-based GNN encoder [17]. Specifically, it uses 13 motif-based adjacency matrices to capture the high-order structure of a gene pair’s neighborhood, followed by a GNN with injective concatenation to combine motif-wise representations and produce the final representation of the core graph. We summarize our key contributions in the following.

- We employ the GIB principle to define a core subgraph, providing a principled alternative to attention weights which often exhibit instability and bias toward frequent edges.
- We extend the GIB objective to handle data with multiple core subgraphs, resulting in DGIB, which serves as the objective for our DGIB4SL model.
- We use a motif-based GNN encoder in DGIB4SL to capture both low- and high-order structures in node neighborhoods, ensuring reliable high-order structures in explanations.
- Experimental results demonstrate that our DGIB4SL outperforms state-of-the-art methods in both accuracy and explanation diversity.

## Related work

SL prediction methods can be categorized into three types: statistical inference methods, network-based methods, and supervised machine learning methods [18]. Statistical methods [19, 20, 21, 22], such as ASTER [22], rely on predefined biological rules, which limit their applicability in complex systems due to strong underlying assumptions [23, 24, 25]. Network-based approaches [26, 27, 28], such as iMR-gMCSs [28], improved reproducibility by analyzing pathway level interactions. However, their performance is often limited by noise and incomplete data. With advancements in machine learning (ML), supervised techniques such as SVM [29] and RF [30], and their combination [31] have been developed to facilitate feature selection using manually crafted biological features. However, their dependency on manual feature engineering poses the risk of overlooking critical interactions. SL<sup>2</sup>MF [23] advances SL prediction by decomposing SL networks into matrices, offering a structured approach. However, its reliance on linear matrix decomposition struggles to capture the inherent complexity of SL networks. To overcome these limitations, deep learning methods [32, 33, 34, 35, 36, 37, 38, 39, 40, 41] are developed. For example, DDGCN [32], the first GNN-based model, employs GCNs with dual-dropout to mitigate SL data sparsity. Similarly, MPASL [39] improves gene representations by capturing SL interaction preferences and layer-wise differences on heterogeneous graphs. Although many SL gene pairs have been identified, few of them have been applied to cancer treatment. Understanding the underlying biological mechanisms is crucial for developing SL-based cancer therapies. Unfortunately, most ML models lack the capability to fully explain SL mechanisms. To address this, methods incorporating prior knowledge into the above models through knowledge graph (KG) have been proposed [3, 4, 38, 5, 6]. Most of these methods utilize attention mechanisms to identify important edges [3, 4], paths [5], or factors (subsets of relational features) [6] within KG to explain the mechanisms underlying SL. For example, KR4SL [5] encodes structural information, textual semantic information, and sequential semantics to generate gene representations and leverages attention to highlight important edges across hops to form paths as

explanations. Similarly, SLGNN [6] focuses exclusively on KG data for factor-based gene representation learning, where relational features in the KG constitute factors, and attention weights are used to identify the most significant ones. However, attention weights are often unstable, frequently assigning higher weights to frequent edges [11], and typically provide only a single explanation per sample. Additionally, these methods struggle to capture high-order structures for prediction. To address these issues, DGIB4SL replaces attention mechanisms with graph information bottlenecks to identify key edges and employs motif-based encoders along with DPP to encode high-order structures and generate multiple explanations. For further details on explainability in GNNs, please refer to our Appendix.

## Preliminaries

### Notations and problem formulation

An undirected SL graph is denoted by  $G^{\text{SL}} = (\mathcal{V}^{\text{SL}}, \mathcal{Y}^{\text{SL}}, X^{\text{SL}})$ , with the set of nodes (or genes)  $\mathcal{V}^{\text{SL}}$ , the set of edges or SL interactions  $\mathcal{Y}^{\text{SL}}$  and the node feature matrix  $X^{\text{SL}} \in \mathbb{R}^{|\mathcal{V}^{\text{SL}}| \times d_0}$ . In addition to the SL interactions, we also have external knowledge about the functions of genes. We represent this information as a directed Knowledge Graph (KG)  $G^{\text{KG}} = \{(h, r, t) | h, t \in \mathcal{V}^{\text{KG}}, r \in \mathcal{R}^{\text{KG}}\}$  and let  $X^{\text{KG}}$  denote the node features associated with  $G^{\text{KG}}$ , where  $\mathcal{V}^{\text{KG}}$  is a set of entities, and  $\mathcal{R}^{\text{KG}}$  is a set of relations. To achieve the goals outlined later, we define  $G = (A, X, E)$ , where  $A$  is the adjacency matrix,  $X \in \mathbb{R}^{|\mathcal{V}^{\text{SL}} \cup \mathcal{V}^{\text{KG}}| \times d_0}$  is the node feature matrix and  $E \in \mathbb{R}^{|\mathcal{R}^{\text{KG}} \cup \{\text{"SL"}\}| \times d_1}$  is the edge feature matrix. Graph  $G$  represents the directed *joint graph* of  $G^{\text{SL}}$  and  $G^{\text{KG}}$ , constructed by mapping genes from  $G^{\text{SL}}$  to entities in  $G^{\text{KG}}$ , and adding edges labeled "SL" for corresponding gene pairs based on  $G^{\text{SL}}$ . We use  $(T)_{ij}$  to represent the element at the  $i$ -th row and the  $j$ -th column of a matrix  $T$ , and  $(T)_{i*}$  to represent the  $i$ -th row of the matrix. A comprehensive list of the mathematical notations used in this paper is provided in Table S1 in the Appendix.

In this paper, we investigate the problem of interpretable synthetic lethality prediction, which aims to extract a local subgraph around two target genes for link prediction, potentially in an end-to-end fashion. Formally, given the joint graph  $G$  that combines the SL graph and the KG, and a pair of genes  $u$  and  $v$ , we first collect their  $t$ -hop neighborhoods from  $G$  for each gene,  $\mathcal{N}_t(u) = \{s | \text{dist}(s, u) \leq t\}$ ,  $\mathcal{N}_t(v) = \{s | \text{dist}(s, v) \leq t\}$ , where  $\text{dist}(\cdot, \cdot)$  denotes the shortest distance between two nodes. We then take the intersection of nodes between their neighborhoods to construct a pairwise **enclosing graph** [4]  $G^{uv} = \{(i, r, j) | i, j \in \mathcal{N}_t(u) \cap \mathcal{N}_t(v), r \in \mathcal{R}^{\text{KG}} \cup \{\text{"SL"}\}\}$ . Our goal is to learn a function  $f : \{G^{uv} | u, v \in \mathcal{V}^{\text{SL}}\} \rightarrow \{\tilde{G}^{uv} | \tilde{G}^{uv} \subseteq G^{uv}\}$ , which maps the enclosing graphs  $G^{uv}$  to optimized subgraph  $\tilde{G}^{uv}$ , and learn a binary classifier  $g_\theta(\tilde{G}^{uv})$  parameterized by  $\theta$  for SL prediction based on the optimized subgraph  $\tilde{G}^{uv}$ .

### Information bottleneck

In machine learning, it is crucial to determine which parts of the input data should be preserved and which should be discarded. Information bottleneck (IB) [42] offers a principled approach for addressing this challenge by compressing the source random variable to keep the information relevant for predicting the target random variable and discarding target-irrelevant information.

**Definition 1** (Information Bottleneck (IB)). Given random variables  $Q$  and  $Y$ , the Information Bottleneck principle aims to compress  $Q$  to a bottleneck random variable  $B$ , while keeping the information relevant for predicting  $Y$ :

$$\min_B \underbrace{-I(Y; B)}_{\text{Prediction}} + \underbrace{\beta I(Q; B)}_{\text{Compression}}, \quad (1)$$

where  $\beta > 0$  is a Lagrangian multiplier to balance the two mutual information terms.

Recently, the IB principle has been applied to learn a bottleneck graph named IB-Graph for the input graph [12], which keeps *minimal sufficient information* in terms of the graph's data. In our context of SL prediction, the IB-Graph is defined as follows.

**Definition 2** (IB-Graph). For an enclosing graph  $G^{uv} = (A^{uv}, X^{uv}, E^{uv})$  around a pair of genes  $u$  and  $v$  and the associated label information  $Y$ , the optimal subgraph  $\tilde{G}^{uv} = (\tilde{A}^{uv}, \tilde{X}^{uv})$  found by Information Bottleneck principle is called IB-Graph if

$$\tilde{G}^{uv} = \arg \min_{\tilde{G}^{uv}} \underbrace{-I(Y; \tilde{G}^{uv}) + \beta I(G^{uv}; \tilde{G}^{uv})}_{\text{Graph Information Bottleneck, GIB}}, \quad (2)$$

where  $\tilde{A}^{uv}$  and  $\tilde{X}^{uv}$  are the task-relevant adjacency matrix and the node feature matrix of  $\tilde{G}^{uv}$ , respectively.

Intuitively, GIB (Eq. 2) aims to learn the core subgraph of the input graph  $G^{uv}$ , discarding information from  $G^{uv}$  by minimizing the mutual information  $I(G^{uv}; \tilde{G}^{uv})$ , while preserving target-relevant information by maximizing the mutual information  $I(Y; \tilde{G}^{uv})$ .

## Methods

### Overview

In this section, we present Diverse Graph Information Bottleneck for Synthetic Lethality (DGIB4SL), an interpretable SL prediction framework that incorporates a diversity constraint using Determinantal Point Process (DPP) and GIB objective to generate multiple explanations called IB-graphs for the same gene pair. The framework consists of three key components: IB objective formulation, motif-based DGIB estimation, and prediction. First, we introduce our DGIB objective and derive its tractable upper bound. Next, given that most of the existing IB estimation approaches fail to capture high-order structure information, we propose a novel motif-based DGIB estimation method, which involves three phases: IB-graph learning through random noise injection to select significant edges, graph representation learning (GRL), and prediction, as shown in Fig. 2(a)-(c). In the GRL phase, we employ the motif-wise representation learning method [17] to implement the GNN module in Fig. 2(b), enabling the capture of high-order structures in IB-graph, as illustrated in Fig. 2(d).

### Diverse graph information bottleneck

We now present our main result, which demonstrates how to generate  $K \geq 1$  different IB-graphs for any gene pair  $(u, v)$ , denoted as  $\{\tilde{G}_1^{uv}, \dots, \tilde{G}_K^{uv}\}$ . We first reduce this problem to a special case of the *subset selection problem* where diversity is preferred, i.e., the problem of balancing two aspects: (i) each

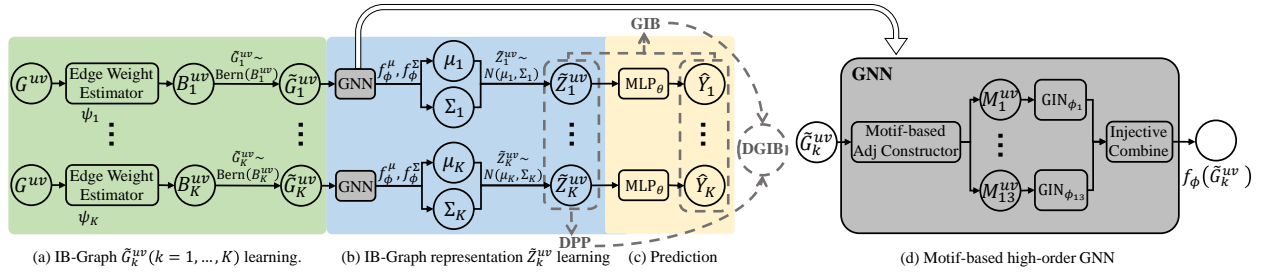


**Fig. 2.** Overview of DGIB4SL. DGIB4SL takes the enclosing graph data  $G^{uv} = (A^{uv}, X^{uv}, E^{uv})$  around genes  $u$  and  $v$  as inputs, throughout the phases (a),(b), and (c), and outputs the interaction confidence of the gene pair  $(u, v)$  and  $K$  IB-graphs  $\tilde{G}_1^{uv}, \dots, \tilde{G}_K^{uv}$  that captures the high-order graph structure. In phase (a), an IB-graph  $\tilde{G}_k^{uv}$  is generated by injecting random noise to select important edges, with edge weights  $B_k^{uv}$  estimated from  $G^{uv}$  using the edge weight estimation module (Eq. S11).  $B_k^{uv}$  serves as the parameter for a multi-dimensional Bernoulli distribution, from which an adjacency matrix of  $\tilde{G}_k^{uv}$  is sampled. In phase (b), IB-graph representations are learned via variational estimation. Each IB graph data  $\tilde{G}_k^{uv}$  is passed through the same motif-based GNN  $f_\phi$  (Eq. 10) to obtain a distribution from which a representation  $\tilde{Z}_k^{uv}$  is sampled. The motif-based GNN, shown in subfigure (d), projects the IB-graph into 13 motif-based matrices. Each motif-based matrix  $M_k^{uv}$  is processed by a different GIN encoder to produce motif-wise representations, which are then concatenated (Eq. 15). In phase (c), each IB-graph representation is passed through an MLP-based classifier to make  $K$  predictions (Eq. 11). During training, the representations and predictions are used to compute DPP and GIB, which are jointly optimized in DGIB4SL.

selected subgraph should satisfy the definition of an IB-Graph; and (ii) the selected subgraphs should be diverse as a group so that the subset is as informative as possible.

Determinantal Point Process (DPP) [16] is an elegant and effective probabilistic model designed to address one key aspect of the above problem: diversity. Formally, let  $\mathcal{G}^{uv}$  denote the set of all possible subgraphs of a graph  $G^{uv}$ . A point process  $P$  defined on the ground set  $\mathcal{G}^{uv}$  is a probability measure over the power set of  $\mathcal{G}^{uv}$ .  $P$  is called a DPP if, for any subset  $\{\tilde{G}_1^{uv}, \dots, \tilde{G}_K^{uv}\} \subseteq \mathcal{G}^{uv}$ , the probability of selecting this subset is given by

$$P(\{\tilde{G}_1^{uv}, \dots, \tilde{G}_K^{uv}\}) \propto \det(L^{uv}), \quad (3)$$

where  $\det(\cdot)$  represents the determinant of a given matrix and  $L^{uv} \in \mathbb{R}^{K \times K}$  is a real, positive semidefinite (PSD) matrix and thus there exists a matrix  $U \in \mathbb{R}^{K \times d_3}$  such that

$$L^{uv} = UU^T, (U)_k = \text{GRL}(\tilde{G}_k^{uv}), \quad (4)$$

where  $(U)_k \in \mathbb{R}^{d_3}$  is the graph representation of the  $k$ -th IB-graph  $\tilde{G}_k^{uv}$  and GRL denotes the graph representation learning module. More details about the GRL module and intuitions about the ability of Eq. 3 to measure diversity are provided in Eqs. 9-12 and Appendix, respectively.

To learn  $K$  different subgraphs from the enclosing graph  $G^{uv}$  for the gene pair  $(u, v)$  that balance diversity with the IB-graph definition, we introduce the Diverse Graph Information Bottleneck (DGIB) objective function, formulated as follows:

$$\min_{\tilde{G}_1^{uv}, \dots, \tilde{G}_K^{uv}} \frac{1}{K} \sum_{k=1}^K \underbrace{-I(Y; \tilde{G}_k^{uv})}_{\text{Graph Information Bottleneck}} + \beta_1 \underbrace{I(G^{uv}; \tilde{G}_k^{uv})}_{\text{DPP}} - \beta_2 \underbrace{\det(L^{uv})}_{\text{DPP}}, \quad (5)$$

where  $\beta_2 > 0$  is a Lagrangian multiplier to trade off GIB and DPP terms. Intuitively, the GIB term focuses on learning multiple IB-graphs from the input graph  $G^{uv}$ , while the DPP term ensures that these IB-graphs are as different as possible.

Due to the non-Euclidean nature of graph data and the intractability of mutual information, it is challenging to optimize the DGIB objective in Eq. 5 directly. Therefore, we adopt the approach of Sun et al. [43] to derive tractable

variational upper bounds for  $-I(Y; \tilde{G}_k^{uv})$  and  $I(G^{uv}; \tilde{G}_k^{uv})$ :

$$\begin{aligned} \min_{\tilde{G}_1^{uv}, \dots, \tilde{G}_K^{uv}} \frac{1}{K} \sum_{k=1}^K \underbrace{-\mathbb{E}_{Y, \tilde{G}_k^{uv}} [\log q_\theta(Y | \tilde{G}_k^{uv})]}_{\text{Upper bound of } -I(Y; \tilde{G}_k^{uv})} \\ + \beta_1 \frac{1}{K} \sum_{k=1}^K \underbrace{\mathbb{E}_{G^{uv}} [D_{\text{KL}}(q_\phi(\tilde{G}_k^{uv} | G^{uv}) || q(\tilde{G}_k^{uv}))]}_{\text{Upper bound of } I(G^{uv}; \tilde{G}_k^{uv})} \\ - \beta_2 \det(L^{uv}). \end{aligned} \quad (6)$$

Detailed proof of Eq. 6 is given in Appendix.

**Remark 1:** Each explanation or IB-graph generated by DGIB4SL consists of a single core subgraph rather than a combination of multiple core subgraphs. In datasets with tens of thousands of gene pairs, as used in our experiments, individual core subgraphs are more likely to be shared across different enclosing graphs than combinations of multiple core subgraphs. This is because the probability of a specific combination being repeatedly shared decreases exponentially with its complexity. In contrast, the structural simplicity of individual core subgraphs makes them more likely to be shared. Minimizing the compression term in DGIB allows DGIB4SL to select individual core subgraphs with higher shared frequency.

### High-order motif-based DGIB estimation

We now address another key question of this work: how to compute the DGIB upper bound in Eq. 6 without losing the high-order information, which is crucial for generating trustworthy explanations. For instance, in a KG, a gene's functional relevance often depends on high-order structures, such as cooperative pathways or shared regulatory targets among its neighbors. Ignoring these structures can result in misleading explanations. To overcome this, we propose a novel high-order motif-based DGIB estimation method DGIB4SL.

#### Mutual information estimation

We first outline the general procedure for estimating the DGIB upper bound defined in Eq. 6 which is largely analogous to previous work [44, 43]. This procedure involves learning the  $k$ -th IB-graph  $\tilde{G}_k^{uv}$  from the enclosing graph  $G^{uv}$  and driving

its representation  $\tilde{Z}_k^{uv} \in \mathbb{R}^{d_3}$  through a graph representation learning function (GRL), such that  $\tilde{Z}_k^{uv} = \text{GRL}(\tilde{G}_k^{uv})$ , assuming no information is lost during this transformation. Under this assumption,  $I(Y; \tilde{Z}_k^{uv}) \approx I(Y; \tilde{G}_k^{uv})$ ,  $I(G^{uv}; \tilde{Z}_k^{uv}) \approx I(G^{uv}; \tilde{G}_k^{uv})$ . Consequently, the DGB upper bound, which DGB4SL aims to minimize, is expressed as:

$$\begin{aligned} \min_{\tilde{G}_1^{uv}, \dots, \tilde{G}_K^{uv}} & -\frac{1}{K} \sum_{k=1}^K \mathbb{E}_{Y, \tilde{G}_k^{uv}} [\log q_\theta(Y | \tilde{Z}_k^{uv})] - \beta_2 \det(L^{uv}) \\ & + \beta_1 \frac{1}{K} \sum_{k=1}^K \mathbb{E}_{G^{uv}} [D_{\text{KL}}(q_\phi(\tilde{Z}_k^{uv} | G^{uv}) || q(\tilde{Z}_k^{uv}))] \end{aligned} \quad (7)$$

To calculate Eq. 7, we follow a two-step process. In **Step 1**, we estimate a IB-graph  $\tilde{G}_k^{uv}$  based on all the subgraphs from  $G^{uv}$ . In **Step 2**, we implement the GRL function to infer the graph representation  $\tilde{Z}_k^{uv}$  of  $\tilde{G}_k^{uv}$  and feed  $\tilde{Z}_k^{uv}$  into Eq. 7.

**(Step 1: IB-graph  $\tilde{G}_k^{uv}$  Learning)** We compress the information of  $G^{uv} = (A^{uv}, X^{uv}, E^{uv})$  via noise injection to estimate the  $k$ -th IB-graph  $\tilde{G}_k^{uv} = (\tilde{A}_k^{uv}, \tilde{X}_k^{uv})$ . To construct  $\tilde{A}_k^{uv}$ , we model all potential edges of the subgraph as mutually independent Bernoulli random variables. The parameters of these variables are determined by the learned important weights  $B_k^{uv} \in \mathbb{R}^{|\mathcal{V}^{uv}| \times |\mathcal{V}^{uv}|}$ , where  $\mathcal{V}^{uv}$  denotes the set of entities in  $G^{uv}$ :

$$\tilde{A}_k^{uv} = \bigcup_{i,j \in \mathcal{V}^{uv}} \left\{ (\tilde{A}_k^{uv})_{i,j} \sim \text{Bernoulli}((B_k^{uv})_{i,j}) \right\}, \quad (8)$$

where  $(B_k^{uv})_{i,j}$  represents the importance weight or sampling probability for the entity pair  $(i, j)$ . The computation of  $B_k^{uv}$  (corresponding to  $\psi_k$  in Figure 1) is jointly optimized with relational graph learning, following the approach of Wang et al. [45]. Further details are provided in Appendix. To sample the IB-graph, we employ the concrete relaxation [46] for the Bernoulli distribution. Additionally, we construct  $\tilde{X}_k^{uv}$  to be the same as  $X^{uv}$  since no nodes are removed during the construction of  $\tilde{A}_k^{uv}$ . An example of the IB-graph construction is provided in the Appendix.

**(Step 2: IB-Graph Representation Learning and Prediction)** Using the previously constructed  $\tilde{G}_k^{uv} = (\tilde{A}_k^{uv}, \tilde{X}_k^{uv})$ , we compute the prediction, diversity and KL terms in Eq. 7 by implementing  $\tilde{Z}_k^{uv} = \text{GRL}(\tilde{G}_k^{uv})$  through variational inference. For the KL term  $D_{\text{KL}}(q_\phi(\tilde{Z}_k^{uv} | G^{uv}) || q(\tilde{Z}_k^{uv}))$ , we treat the prior  $p(\tilde{Z}_k^{uv})$  and the posterior  $q_\phi(\tilde{Z}_k^{uv} | G^{uv})$  as parametric Gaussians and thus this term has an analytic solution:

$$\begin{aligned} p(\tilde{Z}_k^{uv}) & := N(\mu_0, \Sigma_0), \\ q_\phi(\tilde{Z}_k^{uv} | G^{uv}) & := N(f_\phi^\mu(\tilde{A}_k^{uv}, \tilde{X}_k^{uv}), f_\phi^\Sigma(\tilde{A}_k^{uv}, \tilde{X}_k^{uv})), \end{aligned} \quad (9)$$

where the outputs  $f_\phi^\mu(\cdot) \in \mathbb{R}^{d_3}$  and  $f_\phi^\Sigma(\cdot) \in \mathbb{R}^{d_3 \times d_3}$  represent the mean vector and the diagonal covariance matrix of the distribution for the graph embedding  $\tilde{Z}_k^{uv} \in \mathbb{R}^{d_3}$  of  $\tilde{G}_k^{uv}$ , respectively. We model  $f_\phi(\cdot)$  as a GNN parameterized by the weights  $\phi$  with  $2d_3$ -dimensional output and a readout or pooling operator. The first  $d_3$  dimensions of this GNN's output correspond to  $f_\phi^\mu(\cdot)$ , while the remaining  $d_3$  dimensions correspond to  $f_\phi^\Sigma(\cdot)$ , formally expressed as:

$$(f_\phi^\mu(\tilde{A}_k^{uv}, \tilde{X}_k^{uv}), f_\phi^\Sigma(\tilde{A}_k^{uv}, \tilde{X}_k^{uv})) = \text{readout}(\text{GNN}(\tilde{A}_k^{uv}, \tilde{X}_k^{uv}; \phi)). \quad (10)$$

We treat  $p(\tilde{Z}_k^{uv}) := N(\mathbf{0}, I)$  as a fixed  $d_3$ -dimensional spherical Gaussian distribution. To compute the prediction term  $\mathbb{E}_{Y, \tilde{G}_k^{uv}} [\log q_\theta(Y | \tilde{Z}_k^{uv})]$ , we adopt the equivalent cross entropy loss function  $L^{\text{CE}}$ . The conditional distribution  $q_\theta(Y | \tilde{Z}_k^{uv})$  is implemented using a 2-layer perceptron in this work,

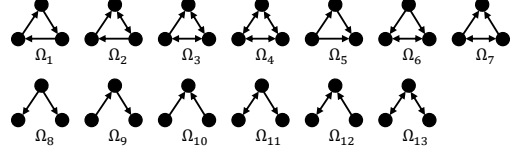


Fig. 3. All 3-node motifs in a directed and unweighted graph.

parameterized by trainable weights  $\theta$ , as described below.

$$-\mathbb{E}_{Y, \tilde{G}_k^{uv}} [\log q_\theta(Y | \tilde{Z}_k^{uv})] = L^{\text{CE}}(Y, \text{MLP}(\tilde{Z}_k^{uv}; \theta)). \quad (11)$$

Finally, for the diversity term  $\det(L^{uv}) = \det(UU^T)$  (Eq. 7, Eq. 4), the matrix  $U$  is constructed by arranging the  $K$  IB-graph representations as its rows. Specifically,

$$U = (\tilde{Z}_1^{uv}, \dots, \tilde{Z}_K^{uv})^T. \quad (12)$$

### Generating high-order graph representation via motif

Most methods struggle to satisfy the no-information-loss assumption of the above mutual information estimation framework, since their GNN implementation in Eq.10 often fails to capture the high-order structure of the estimated explanation. Inspired by MGNN [17], we reduce this to a problem of enhancing the model's representation power beyond the 1-dimensional Weisfeiler-Leman (1-WL) graph isomorphism test [47]. Specifically, the 1-WL test distinguishes graph structures by iteratively compressing node neighborhood information into unique labels, making it a widely recognized tool for evaluating the expressive power of GNNs [47, 48, 17].

We first formalize three key definitions underlying our approach, starting with the notion of a network motif.

**Definition 3** (Network motif). A motif is a connected graph of  $d_5$  nodes ( $d_5 > 1$ ), with a  $d_5 \times d_5$  adjacency matrix  $C$  containing binary elements  $\{0, 1\}$ .

Let  $\Omega_i$  denote different motifs and  $C_i$  represent the corresponding associated matrices. An example of all possible 3-node motifs is shown in Fig.3. Chen et al. [17] demonstrated that 3-node motifs are sufficiently expressive to capture graph structures. Thus, we only use motifs with 3 nodes in this work.

**Definition 4** (Motif set). The motif set of a 3-node motif  $\Omega_i$  in a directed graph  $G = (A, X)$  is defined by

$$\mathcal{M}_i = \{V | V \in \mathcal{V}^3, A^V = C_i\}, \quad (13)$$

where  $V$  is a tuple containing 3 node indices and  $A^V$  is the  $d_5 \times d_5$  adjacency matrix of the subgraph induced by  $V$ .

For example, the motif set of  $\Omega_5$  in Fig. 1 can be  $\{(\text{HR}, \text{Trapped replication fork}, \text{DNA damage}), (\text{HR}, \text{DSB}, \text{DNA damage})\}$ . Based on the motif set, we define the operator  $\text{set}(\cdot)$  to transform an ordered tuple into an unordered set, e.g.,  $\text{set}((v_1, \dots, v_3)) = \{v_1, \dots, v_3\}$ . Using this operator, the motif-based adjacency matrix is defined as follows.

**Definition 5** (Motif-based adjacency matrix). For a graph  $G = (A, X)$ , a motif-based adjacency matrix  $M_i$  of  $G$  in terms of a given motif  $\Omega_i$  is defined by

$$(M_i)_{j,t} = \sum_{V \in \mathcal{M}_i} \mathbb{I}(\{j, t\} \subset \text{set}(V)). \quad (14)$$

Intuitively,  $(M_i)_{j,l}$  denotes the number of times nodes  $j$  and  $l$  are connected through an element of the given motif set  $\mathcal{M}_i$ . The roles of these definitions will be discussed in Eq. 15.

To generate graph embeddings with greater expressive power than the 1-WL test, Chen et al. [17] demonstrated that associating node or graph embeddings with different motif structures and combining these embeddings using an injective function effectively captures high-order and low-order graph structure. Specifically, we use a 2-layer GIN [47] as the underlying GNN and employ different GINs to encode the structure of 13 motifs in  $\tilde{G}^{uv}$ , producing node embeddings through motif-based adjacency matrices. Then, the motif-wise embeddings are combined via injective concatenation. Mathematically, we construct the GNN module in Eq. 15 as

$$\text{GNN}(\tilde{A}_k^{uv}, \tilde{X}_k^{uv}; \phi) := \parallel_{i=1}^{13} \text{GIN}(M_i^{uv}, \tilde{X}_k^{uv}; \phi_i), \quad (15)$$

where  $M_i^{uv}$  are the motif-based adjacency matrix of  $\tilde{G}^{uv} = (\tilde{A}_k^{uv}, \tilde{X}_k^{uv})$  in terms of a given motif  $\Omega_i$  and  $\parallel$  denotes a concatenation function. In summary, Eq. 15 preserves high-order and low-order pair-wise structural information when calculating DGIB, enhancing the reliability of the high-order structure in an IB-graph.

## Results

### Experimental setup

#### Datasets and baselines

To evaluate the effectiveness of our DGIB4SL, we utilized the dataset provided by the Synthetic Lethality Benchmark (SLB) [49]. The dataset is collected from SynLethDB 2.0, a comprehensive repository of SL data, and includes 11 types of entities and 27 relationships. It contains 35,913 human SL gene pairs involving 9,845 genes, along with a KG named SynLethKG, which comprises 54,012 nodes and 2,233,172 edges. Additional details on SynLethKG can be found in Tables S2–S3 in Appendix.

We evaluated two categories of methods, selecting thirteen recently published methods. These include three matrix factorization (MF)-based methods: GRSMF [25], SL2MF [23], and CMFW [24], and ten GNN-based methods: DDGCN [32], GCATSL [35], SLMGAE [36], MGE4SL [34], PTGNN [37], KG4SL [3], PiLSL [4], NSF4SL [38], KR4SL [5], and SLGNN [6]. Among these, KG4SL, PiLSL, NSF4SL, KR4SL, and SLGNN integrate knowledge graphs (KGs) into the generation of node representations. Detailed descriptions of these baselines can be found in Appendix.

#### Implementation details

We evaluated our method using 5-fold cross-validation by splitting the gene pairs and using 4 ranking metrics: Normalized Discounted Cumulative Gain (NDCG@C), Recall@C, Precision@C, and Mean Average Precision (MAP@C). NDCG@C measures the positioning of known SL gene pairs within the model’s predicted list, while Recall@C and Precision@C assess the model’s ability to identify relevant content and rank the top C results accurately, respectively. MAP@C provides a comprehensive evaluation by combining precision and ranking across multiple queries, averaging the precision at each relevant prediction up to the C-th position. In this study, we evaluated these metrics using the top C=10 and top C=50 predictions. The coefficients  $\beta_1$  and  $\beta_2$  in Eq. 6 were set  $\beta_1 = \beta_2 = 10^{-4}$ . More details on data preprocessing, hyperparameters settings

for DGIB4SL and baseline implementations are provided in Appendix.

### Performance evaluation

We evaluated the empirical performance of DGIB4SL against state-of-the-art baselines, as summarized in Table 2. Baseline performance was referenced from the public leaderboards provided by SLB [49], except for KR4SL, which was based on our experimental results. As shown in Table 2, DGIB4SL consistently outperformed all baselines on the SynLethDB 2.0 dataset [50]. Specifically, KR4SL achieved the second best performance on NDCG@50, Recall@10, Precision@10, Precision@50, MAP@10 and MAP@50, while PiLSL and NSF4SL achieved the second best performance on NDCG@10 and Recall@50, respectively. Our DGIB4SL further improved over KR4SL by 9.9%, 26.7%, 10.6%, 8.0%, 6.0% and 5.5% on NDCG@50, Recall@10, Precision@10, Precision@50, MAP@10 and MAP@50, respectively, and outperformed PiLSL and NSF4SL by 11.5% and 14.2% in NDCG@10 and Recall@50, respectively. From these results, we draw the following conclusions: (i) the competitive performance of DGIB4SL and KG-based baselines highlights the value of KGs in providing biological context for gene related label prediction. (ii) The integration of motifs significantly enhances model performance by expanding the receptive field and encoding high-order edges into predictions effectively.

### Explanation evaluation

#### Qualitative analysis

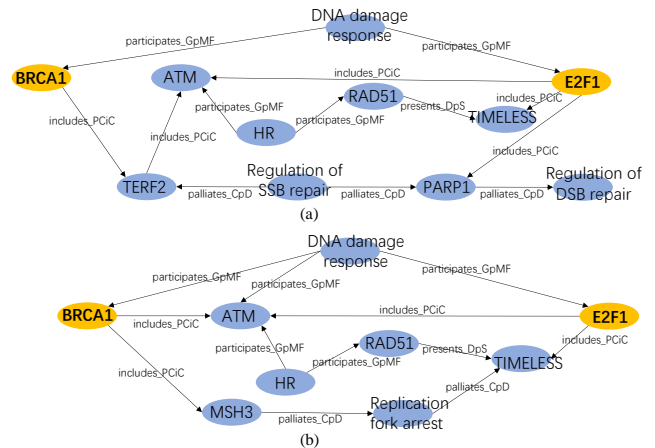


**Fig. 4.** Two explanations learned from our DGIB4SL, provide different insights into the biological mechanisms underlying SL of the same gene pair (BRCA1, E2F1). For details on the edge nomenclature, please refer to Table S4 in Appendix.

Leveraging the DGIB mechanism (Eq. 6), our DGIB4SL not only predicts SL interactions but also provides  $K \geq 1$  explanations that reveal the biological mechanisms underlying the predictions for the same gene pair. For this case study, we selected the SL pair BRCA1 and E2F1 from the test data, where the predicted interaction between BRCA1 and E2F1 matched the actual label. To remove unimportant edges from the enclosing core graphs of (BRCA1, E2F1), we applied edge sampling probabilities with thresholds 0.58 and 0.76 for the first and second core subgraphs distribution

**Table 1.** Performance of various methods in terms of NDCG and Recall under 5-fold cross-validation. The best results are highlighted in bold, while the second-best results are underlined. Values in parentheses indicate paired  $t$ -test  $p$ -values comparing baselines with DGIB4SL.

	NDCG@10	NDCG@50	Recall@10	Recall@50
GRSMF [25]	0.2844 ( $2.06 \times 10^{-7}$ )	0.3153 ( $9.20 \times 10^{-9}$ )	0.3659 ( $8.04 \times 10^{-7}$ )	0.4460 ( $3.07 \times 10^{-4}$ )
SL <sup>2</sup> MF [23]	0.2807 ( $7.79 \times 10^{-8}$ )	0.3110 ( $7.49 \times 10^{-8}$ )	0.2642 ( $8.44 \times 10^{-7}$ )	0.3401 ( $2.95 \times 10^{-7}$ )
CMFW [24]	0.2390 ( $1.24 \times 10^{-7}$ )	0.2744 ( $7.16 \times 10^{-7}$ )	0.3257 ( $2.15 \times 10^{-6}$ )	0.4097 ( $4.14 \times 10^{-5}$ )
DDGCN [32]	0.1568 ( $1.94 \times 10^{-7}$ )	0.1996 ( $6.74 \times 10^{-8}$ )	0.2379 ( $7.61 \times 10^{-9}$ )	0.3447 ( $2.76 \times 10^{-5}$ )
GCATSL [35]	0.2642 ( $3.99 \times 10^{-7}$ )	0.2976 ( $1.24 \times 10^{-6}$ )	0.3363 ( $5.91 \times 10^{-6}$ )	0.4203 ( $3.67 \times 10^{-4}$ )
SLMGAE [36]	0.2699 ( $6.63 \times 10^{-7}$ )	0.3160 ( $1.19 \times 10^{-6}$ )	0.3198 ( $1.26 \times 10^{-5}$ )	0.4421 ( $1.26 \times 10^{-3}$ )
MGE4SL [34]	0.0028 ( $2.66 \times 10^{-9}$ )	0.0071 ( $4.89 \times 10^{-9}$ )	0.0020 ( $1.35 \times 10^{-8}$ )	0.0085 ( $6.13 \times 10^{-9}$ )
PTGNN [37]	0.2358 ( $1.07 \times 10^{-7}$ )	0.2740 ( $6.66 \times 10^{-7}$ )	0.3361 ( $9.43 \times 10^{-6}$ )	0.4323 ( $1.96 \times 10^{-4}$ )
KG4SL [3]	0.2505 ( $1.04 \times 10^{-6}$ )	0.2853 ( $1.05 \times 10^{-7}$ )	0.3347 ( $4.40 \times 10^{-7}$ )	0.4253 ( $2.48 \times 10^{-5}$ )
PiLSL [4]	<u>0.5166</u> ( $3.32 \times 10^{-5}$ )	0.5175 ( $3.28 \times 10^{-5}$ )	0.3970 ( $3.99 \times 10^{-6}$ )	0.4021 ( $3.82 \times 10^{-6}$ )
NSF4SL [38]	0.2279 ( $2.65 \times 10^{-6}$ )	0.2706 ( $4.50 \times 10^{-7}$ )	0.3526 ( $2.96 \times 10^{-5}$ )	<u>0.4624</u> ( $1.14 \times 10^{-3}$ )
KR4SL [5]	0.5105 ( $2.19 \times 10^{-5}$ )	<u>0.5248</u> ( $5.79 \times 10^{-5}$ )	<u>0.4131</u> ( $6.97 \times 10^{-6}$ )	0.4135 ( $5.62 \times 10^{-6}$ )
SLGNN [6]	0.1468 ( $4.49 \times 10^{-8}$ )	0.2004 ( $1.85 \times 10^{-7}$ )	0.2154 ( $1.90 \times 10^{-7}$ )	0.3717 ( $1.26 \times 10^{-4}$ )
DGIB4SL	<b>0.5760</b>	<b>0.5766</b>	<b>0.5233</b>	<b>0.5280</b>

**Table 2.** Performance of various methods in terms of Precision and MAP under 5-fold cross-validation. The best results are highlighted in bold, while the second-best results are underlined. Values in parentheses indicate paired  $t$ -test  $p$ -values comparing baselines with DGIB4SL.

	Precision@10	Precision@50	MAP@10	MAP@50
GRSMF [25]	0.3683 ( $1.02 \times 10^{-5}$ )	0.4461 ( $1.42 \times 10^{-4}$ )	0.2568 ( $7.15 \times 10^{-7}$ )	0.2521 ( $9.92 \times 10^{-8}$ )
SL <sup>2</sup> MF [23]	0.2694 ( $3.53 \times 10^{-7}$ )	0.3407 ( $3.45 \times 10^{-6}$ )	0.2861 ( $1.35 \times 10^{-7}$ )	0.2769 ( $1.68 \times 10^{-7}$ )
CMFW [24]	0.3267 ( $8.57 \times 10^{-7}$ )	0.4098 ( $4.37 \times 10^{-5}$ )	0.2043 ( $5.65 \times 10^{-7}$ )	0.2069 ( $1.13 \times 10^{-6}$ )
DDGCN [32]	0.2385 ( $1.60 \times 10^{-6}$ )	0.3447 ( $1.41 \times 10^{-5}$ )	0.1280 ( $6.26 \times 10^{-9}$ )	0.1321 ( $3.74 \times 10^{-8}$ )
GCATSL [35]	0.3372 ( $5.36 \times 10^{-6}$ )	0.4204 ( $1.03 \times 10^{-3}$ )	0.2354 ( $8.96 \times 10^{-7}$ )	0.2382 ( $7.66 \times 10^{-8}$ )
SLMGAE [36]	0.3222 ( $3.58 \times 10^{-6}$ )	0.4422 ( $7.76 \times 10^{-4}$ )	0.2514 ( $2.10 \times 10^{-7}$ )	0.2469 ( $9.86 \times 10^{-7}$ )
MGE4SL [34]	0.0022 ( $1.31 \times 10^{-8}$ )	0.0085 ( $8.87 \times 10^{-9}$ )	0.0018 ( $3.17 \times 10^{-9}$ )	0.0024 ( $1.58 \times 10^{-8}$ )
PTGNN [37]	0.3372 ( $2.26 \times 10^{-6}$ )	0.4324 ( $1.48 \times 10^{-4}$ )	0.1948 ( $3.46 \times 10^{-7}$ )	0.1975 ( $1.80 \times 10^{-7}$ )
KG4SL [3]	0.3357 ( $4.68 \times 10^{-6}$ )	0.4254 ( $1.43 \times 10^{-4}$ )	0.2175 ( $1.50 \times 10^{-6}$ )	0.2208 ( $1.04 \times 10^{-6}$ )
PiLSL [4]	0.4098 ( $3.71 \times 10^{-6}$ )	0.4035 ( $3.84 \times 10^{-6}$ )	0.5153 ( $4.95 \times 10^{-4}$ )	0.5149 ( $2.40 \times 10^{-3}$ )
NSF4SL [38]	0.3563 ( $1.34 \times 10^{-5}$ )	0.4626 ( $2.69 \times 10^{-4}$ )	0.1881 ( $1.85 \times 10^{-6}$ )	0.1818 ( $3.65 \times 10^{-6}$ )
KR4SL [5]	<u>0.4845</u> ( $1.50 \times 10^{-4}$ )	<u>0.4901</u> ( $4.75 \times 10^{-4}$ )	<u>0.5175</u> ( $6.82 \times 10^{-4}$ )	<u>0.5200</u> ( $5.33 \times 10^{-3}$ )
SLGNN [6]	0.2172 ( $1.86 \times 10^{-6}$ )	0.3718 ( $5.13 \times 10^{-5}$ )	0.1259 ( $1.16 \times 10^{-7}$ )	0.1252 ( $2.34 \times 10^{-8}$ )
DGIB4SL	<b>0.5359</b>	<b>0.5294</b>	<b>0.5485</b>	<b>0.5484</b>

(Eq. 8), respectively. Edges with probabilities exceeding these thresholds ( $(B_1^{uv})_{i,j} > 0.58$ ,  $(B_2^{uv})_{i,j} > 0.76$ ) were retained. The filtered core graphs are shown in Fig. 4 (a) and (b).

We first analyzed the first core subgraph (Fig. 4(a)). The first core subgraph highlights two key mechanisms of SL between BRCA1 and E2F1: (1) HR Deficiency Due to BRCA1 Mutation: Pathway “BRCA1  $\xrightarrow{\text{includes\_PCiC}}$  TERF2  $\xrightarrow{\text{includes\_PCiC}}$  ATM  $\xleftarrow{\text{participates\_GpMF}}$  HR  $\xrightarrow{\text{participates\_GpMF}}$  RAD51  $\xrightarrow{\text{presents\_DpS}}$  TIMELESS” indicates that BRCA1 mutation inactivates the HR pathway. This leaves double-strand breaks (DSBs), converted from unresolved single-strand breaks (SSBs), unrepaired. (2) SSB Repair Pathway Blockage: The pathways “E2F1  $\xrightarrow{\text{includes\_PCiC}}$  PARP1  $\xrightarrow{\text{palliates\_CpD}}$  Regulation of DSB repair” and “Regulation of SSB repair  $\xrightarrow{\text{palliates\_CpD}}$  PARP1” demonstrate that E2F1 mutation weakens both SSB and DSB repair functions. These combined defects in SSB repair and HR result in unreparable DNA damage, genomic instability, and ultimately cell death. Previous studies [51] have shown that E2F1 depletion impairs HR, disrupting DNA replication and causing DNA damage, further supporting these findings.

We then analyzed the second core subgraph (Fig. 4(b)). The second core subgraph identifies a different mechanism, centered

around replication fork blockage, while maintaining the shared premise of homologous recombination repair pathway loss. Specifically, the pathway “E2F1  $\xrightarrow{\text{includes\_PCiC}}$  TIMELESS  $\xleftarrow{\text{palliates\_CpD}}$  Replication Fork Arrest” reveals that E2F1 mutation destabilizes replication forks, leading to stalled replication. TIMELESS, a downstream target of E2F1, plays a critical role in stabilizing replication forks during DNA replication stress.

**Table 3.** Comparison of attention weights in KG-Based SL prediction methods with explanations in DGIB4SL in terms of Fidelity, Sparsity, and Diversity. Symbols  $\uparrow$  and  $\downarrow$  respectively represent that larger and smaller metric values are better. Values in parentheses indicate paired  $t$ -test  $p$ -values against DGIB4SL.

	Infidelity $\downarrow$	Sparseness $\uparrow$	DPP $\uparrow$
KG4SL	$4.0 \times 10^5 (2 \times 10^{-4})$	0.330 ( $8 \times 10^{-4}$ )	-
PiLSL	$5.7 \times 10^5 (9 \times 10^{-3})$	0.340 ( $4 \times 10^{-4}$ )	-
SLGNN	$1.8 \times 10^6 (1 \times 10^{-9})$	0.120 ( $6 \times 10^{-5}$ )	<u>1.59</u> ( $8 \times 10^{-4}$ )
KR4SL	<u><math>5.8 \times 10^4 (2 \times 10^{-3})</math></u>	<u>0.352</u> ( $7 \times 10^{-4}$ )	-
KR4SL*	<u><math>5.8 \times 10^4 (1 \times 10^{-3})</math></u>	0.326 ( $5 \times 10^{-4}$ )	0.48 ( $7 \times 10^{-4}$ )
DGIB4SL	<b><math>6.2 \times 10^3</math></b>	<b>0.463</b>	<b>1.67</b>

### Quantitative analysis

We evaluated the Infidelity [52] and Sparseness [53] (see Appendix for these metrics descriptions) and used the DPP to evaluate the diversity of explanations generated by DGIB4SL and other explainable SL prediction methods, including KG4SL, PiLSL, SLGNN, and KR4SL. To compare diversity, we introduced KR4SL\*, a variant of KR4SL with a multi-head attention mechanism, since the explainable baselines (except for SLGNN) generate a single explanation using similar attention mechanisms. As shown in Table 3, DGIB4SL outperforms other methods in terms of Infidelity, Sparseness, and DPP. We draw the following conclusions:

- **Diversity:** Despite using multi-head attention, KR4SL\* showed lower DPP values, indicating that multi-head attention alone has a limited capacity for generating diverse explanations. SLGNN’s DPP performance is competitive, due to the inclusion of a distance correlation regularizer that encourages independent factor embeddings, indirectly enhancing diversity.
- **Sparsity:** Baselines employing similar attention mechanisms showed comparable Sparseness values, except for SLGNN, which directly uses learnable weights to estimate the importance of different relational features.
- **Fidelity:** The Infidelity of attention-based methods is relatively low, possibly due to the inherent instability and high-frequency biases of attention mechanisms [7, 8].

### Model analysis

#### Ablation study

As illustrated in Fig. 2, the DGIB (Eq. 6), DPP constraint (third line in Eq. 6) and motif-based graph encoder (Eq. 15) are key components of DGIB4SL. Based on these, we derived the following variants for the ablation study: (1) DGIB4SLw/oM: DGIB4SL without motif information, to assess the impact of motifs. (2) DGIB4SLw/oB: DGIB4SL without the DGIB objective (replacing it with an attention mechanism); (3) DGIB4SLw/oP: DGIB4SL without the DPP constraint (essentially reducing the objective to GIB). To evaluate the contributions of motifs, DGIB and DPP, we compared DGIB4SL against these variants. As shown in Fig. 5, DGIB4SL consistently outperformed DGIB4SLw/oM across all metrics, highlighting the importance of incorporating high-order structures through motifs in SL prediction. Secondly, the performance of DGIB4SLw/oB was comparable to DGIB4SL on all metrics. This result is expected, since DGIB4SLw/oB can still extract label-related input information via attention mechanisms, even if this information may not always faithfully reflect the model’s behavior. Thirdly, DGIB4SLw/oP also achieved comparable performance to DGIB4SL. This is intuitive since, without DPP constraints, DGIB4SLw/oP may find  $K$  similar explanations, which could overlap with one of the  $K$  different explanations found by DGIB4SL. To further compare their explanations, we evaluated their diversity using the DPP measure, calculated as the determinant of  $\tilde{G}_1^{uv}, \dots, \tilde{G}_K^{uv}$  (Eqs. 3-4). As shown in the two rightmost columns of Fig. 5, DGIB4SL produced significantly more diverse explanations compared to DGIB4SLw/oP.

#### Convergence analysis

In this section, we analyze the convergence behavior of DGIB4SL. For clarity, we rewrite the DGIB objective function in Eq. 7 as  $L^{\text{DGIB}} = L^{\text{CE}} + \beta_1 L^{\text{KL}} - \beta_2 L^{\text{DPP}}$ , where  $L^{\text{CE}}$  is

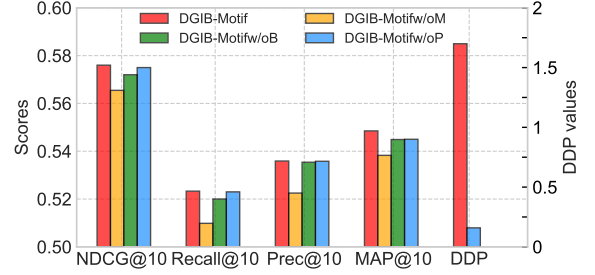


**Fig. 5.** Ablation study of DGIB4SL for Motif, DGIB, and DPP on NDCG@10, Recall@10, Precision@10, MAP@10 (left Y-axis) and one diversity metric DPP (right Y-axis).

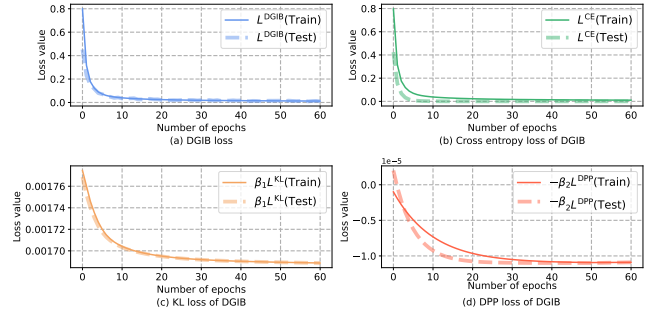


**Fig. 6.** Convergence of DGIB4SL: (a) learning curve of DGIB and (b)-(d): learning curve of each component of the loss of DGIB4SL.

the binary cross-entropy loss,  $\beta_1 L^{\text{KL}}$  is the KL-divergence loss, and  $-\beta_2 L^{\text{DPP}}$  represents the DPP loss. Figure 6 illustrates the convergence trends of each component of the DGIB objective. Solid lines correspond to training set values, while dashed lines represent testing set values. As shown in Fig. 6(a)-(b), both  $L^{\text{DGIB}}$  and  $L^{\text{CE}}$  experienced a steep decline during the initial epochs, with minimal separation between training and testing curves. This indicates rapid learning and effective generalization by the model. In Fig. 6(c),  $L^{\text{KL}}$  shows negligible differences between training and testing curves, suggesting that the compressed input information allows the model to generalize effectively on the test set. In contrast, Fig. 6(d) highlights that  $L^{\text{DPP}}$  initially exhibits a more pronounced gap between training and testing curves. However, this gap narrows over time, demonstrating that the model learns diverse representations effectively, albeit at a slower pace compared to other loss components.

#### Parameter sensitivity

We explored the impact of the Lagrangian multipliers  $\beta_1$  and  $\beta_2$  in Eq. 8, the graph representation dimension  $d_3$  in Eq. 9, and the number of explanations  $K$  generated by DGIB4SL for each gene pair on SL prediction performance. The performance trend is shown in Fig. 7. From the results, we observed the following: (1) As illustrated in Fig. 7(a)-(b), DGIB4SL’s performance was relatively insensitive to  $\beta_1$  and  $\beta_2$ . Specifically,  $\beta_1$  values in the range  $[10^{-6}, 10^{-3}]$  and  $\beta_2$  values in the range  $[10^{-4}, 10^{-2}]$  typically yielded robust and reliable performance. For most cases,  $\beta_1 = \beta_2 = 10^{-4}$  proved to be an optimal choice. (2) Fig. 7(c) indicates that increasing  $d_3$  gradually improved performance, peaking around  $d_3 = 6^4$ , but began to decline afterward, likely due to overfitting. As the performance gain beyond  $d_3 = 6$  was modest, we opted for  $d_3 = 6$ .

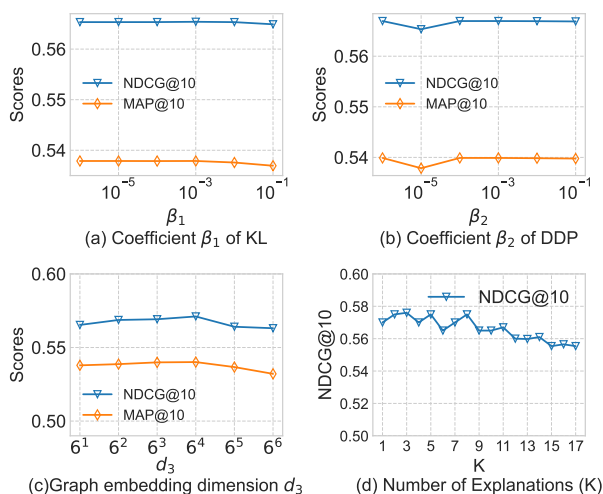


**Fig. 7.** Parameter sensitivity analysis for DGIB4SL on Lagrangian multipliers  $\beta_1$ ,  $\beta_2$ , graph embedding dimension  $d_3$  and the number of explanations  $K$  generated for each gene pair on performance.

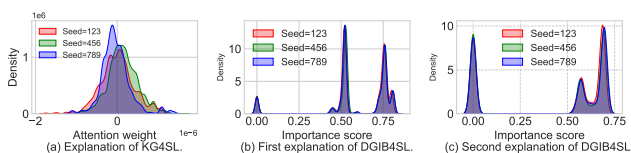


**Fig. 8.** Edge weight distribution of DGIB4SL and KG4SL for the same gene pair (ACTR10, PELO) under different random seeds.

to simplify the model while maintaining strong performance. (3) Fig. 7(d) shows the impact of  $K$  within the approximate range of  $[1, 17]$  (heuristically estimated; see Appendix for details). The results indicate that DGIB4SL performs stably when  $K \leq 9$ , primarily due to two reasons:

- When the actual number of core subgraphs  $c_i$  in the  $i$ -th enclosing graph satisfies  $c_i \geq K$ , DGIB4SL only needs to identify at least one core subgraph to make accurate predictions, and the specific number of identified core subgraphs has minimal impact on the results.
- When  $c_i < K$ , the setting of  $\beta_2 = 10^{-4}$  in DGIB biases the trade-off toward relevance (GIB) over diversity (DPP), causing DGIB4SL to prioritize generating core subgraphs relevant to the labels, even if some explanations may overlap.

For  $K > 9$ , DGIB4SL’s performance declines, primarily due to the increased number of parameters in the relational edge weight module (Eq. S11), which leads to overfitting. We set  $K=3$  for DGIB4SL because most gene pairs have no more than three core subgraphs. This choice helps effectively prevent overfitting and reduce explanation overlap.

### Stability analysis

To evaluate the stability of DGIB4SL and attention-based methods, we introduced noise using three distinct random seeds to compare the edge importance distributions. Specifically, we ran DGIB4SL and KG4SL three times with different random seeds. Here, KG4SL was selected as a representative of attention-based methods due to its straightforward design and interpretability. For each run, kernel density estimation [54]

was applied to compute the distributions of the importance scores for each edge within the core graph of the gene pair (ACTR10, PELO). As shown in Fig. 8(a), the (unnormalized) attention weight distribution generated by KG4SL is unstable. In contrast, Fig. 8(b) and (c) show that the distributions of edge weight (i.e.,  $(B_k^{uv})_{i,j}$  in Eq. 8) generated by DGIB4SL for its two explanations largely overlap across different random seeds, demonstrating the stability of our DGIB4SL’s explainability.

## Conclusion and discussion

We present Diverse Graph Information Bottleneck for Synthetic Lethality (DGIB4SL), an interpretable SL prediction framework that ensures trustworthy and diverse explanations. DGIB4SL introduces a novel DGIB objective with a Determinantal Point Process constraint to enhance diversity and employs a motif-based strategy to capture high-order graph information. A variational upper bound is proposed to address computational challenges, enabling efficient estimation. Experimental results show that DGIB4SL outperforms all baselines on the SynLethDB 2.0 dataset.

A key limitation of DGIB4SL lies in the fixed number  $K$  for generating explanations, which may result in overlapping or incomplete explanations. Future work could explore an adaptive mechanism to dynamically adjust  $K$  for each enclosing graph. Additionally, DGIB4SL is a general framework for interaction prediction and can be applied to other domains requiring diverse and interpretable explanations, such as drug-drug interaction prediction and functional genomics research.

### Key Points:

- We propose an interpretable knowledge graph neural network DGIB4SL that predicts synthetic lethality interactions with diverse explanations.
- We use the GIB principle to define a core subgraph of a gene pair, and extend the GIB objective to handle data with multiple core subgraphs, resulting in DGIB, which serves as the objective for DGIB4SL.
- We apply motif-based GNNs to capture high-order graph structures.
- The model’s effectiveness is validated through real-world data and case studies.

## References

1. Thomas Helleday. The underlying mechanism for the parp and brca synthetic lethality: clearing up the misunderstandings. *Molecular oncology*, 5(4):387–393, 2011.
2. Suzanne Leijen, Robin MJM van Geel, Gabe S Sonke, Daphne de Jong, Efraim H Rosenberg, Serena Marchetti, Dick Pluim, Erik van Werkhoven, Shelonitda Rose, Mark A Lee, et al. Phase ii study of wee1 inhibitor azd1775 plus carboplatin in patients with tp53-mutated ovarian cancer refractory or resistant to first-line therapy within 3 months. *Journal of Clinical Oncology*, 34(36):4354–4361, 2016.
3. Shike Wang, Fan Xu, Yunyang Li, Jie Wang, Ke Zhang, Yong Liu, Min Wu, and Jie Zheng. Kg4sl: knowledge graph

- neural network for synthetic lethality prediction in human cancers. *Bioinformatics*, 37, 2021.
4. Xin Liu, Jiale Yu, Siyu Tao, Beiyuan Yang, Shike Wang, Lin Wang, Fang Bai, and Jie Zheng. Pils: pairwise interaction learning-based graph neural network for synthetic lethality prediction in human cancers. *Bioinformatics*, 38(Supplement\_2):ii106–ii112, 2022.
  5. Ke Zhang, Min Wu, Yong Liu, Yimiao Feng, and Jie Zheng. Kr4sl: knowledge graph reasoning for explainable prediction of synthetic lethality. *Bioinformatics*, 39, 2023.
  6. Yan Zhu, Yuhuan Zhou, Yang Liu, Xuan Wang, and Junyi Li. S1gnn: synthetic lethality prediction in human cancers based on factor-aware knowledge graph neural network. *Bioinformatics*, 39(2):btad015, 2023.
  7. Sofia Serrano and Noah A. Smith. Is attention interpretable? In *ACL 2019*.
  8. Sarah Wiegrefe and Yuval Pinter. Attention is not not explanation. In *EMNLP, 2019*.
  9. Gino Brunner, Yang Liu, Damian Pascual, Oliver Richter, Massimiliano Ciaramita, and Roger Wattenhofer. On identifiability in transformers. In *ICLR 2020*.
  10. Christopher Grimsley, Elijah Mayfield, and Julia R. S. Bursten. Why attention is not explanation: Surgical intervention and causal reasoning about neural models. In *Proceedings of The 12th Language Resources and Evaluation Conference, 2020*.
  11. Yicong Li, Xiangguo Sun, Hongxu Chen, Sixiao Zhang, Yu Yang, and Guandong Xu. Attention is not the only choice: Counterfactual reasoning for path-based explainable recommendation. *IEEE Trans. Knowl. Data Eng.*, 36(9):4458–4471, 2024.
  12. Tailin Wu, Hongyu Ren, Pan Li, and Jure Leskovec. Graph information bottleneck. In *NeurIPS 2022*.
  13. Qingyun Sun, Jianxin Li, Hao Peng, Jia Wu, Xingcheng Fu, Cheng Ji, and S Yu Philip. Graph structure learning with variational information bottleneck. In *AAAI 2022*.
  14. Siqi Miao, Mia Liu, and Pan Li. Interpretable and generalizable graph learning via stochastic attention mechanism. In *ICML 2022*.
  15. Ziqi Pan, Li Niu, Jianfu Zhang, and Liqing Zhang. Disentangled information bottleneck. In *AAAI 2021*.
  16. Alex Kulesza, Ben Taskar, et al. Determinantal point processes for machine learning. *Foundations and Trends® in Machine Learning*, 5(2-3):123–286, 2012.
  17. Xuexin Chen, Ruichu Cai, Yuan Fang, Min Wu, Zijian Li, and Zhifeng Hao. Motif graph neural network. *IEEE Transactions on Neural Networks and Learning Systems*, 2023.
  18. Jing Wang, Qinglong Zhang, Junshan Han, Yanpeng Zhao, Caiyun Zhao, Bawei Yan, Chong Dai, Lianlian Wu, Yuqi Wen, Yixin Zhang, Dongjin Leng, Zhongming Wang, Xiaoxi Yang, Song He, and Xiaochen Bo. Computational methods, databases and tools for synthetic lethality prediction. *Briefings Bioinform.*, 23(3), 2022.
  19. Subarna Sinha, Daniel Thomas, Steven Chan, Yang Gao, Diede Brunen, Damoun Torabi, Andreas Reinisch, David Hernandez, Andy Chan, Erinn B Rankin, et al. Systematic discovery of mutation-specific synthetic lethals by mining pan-cancer human primary tumor data. *Nature communications*, 8(1):15580, 2017.
  20. Chen Yang, Yuchen Guo, Ruolan Qian, Yiwen Huang, Linneng Zhang, Jun Wang, Xiaowen Huang, Zhicheng Liu, Wenxin Qin, Cun Wang, et al. Mapping the landscape of synthetic lethal interactions in liver cancer. *Theranostics*, 11(18):9038, 2021.
  21. Jeannette P Staheli, Maxwell L Neal, Arti Navare, Fred D Mast, and John D Aitchison. Predicting host-based, synthetic lethal antiviral targets from omics data. *NAR Molecular Medicine*, 1(1):ugad001, 2024.
  22. Herty Liany, Aishwarya Jayagopal, Dachuan Huang, Jing Quan Lim, Nur Izzah Nbh, Anand Jeyasekharan, Choon Kiat Ong, and Vaibhav Rajan. Aster: A method to predict clinically relevant synthetic lethal genetic interactions. *IEEE Journal of Biomedical and Health Informatics*, 2024.
  23. Yong Liu, Min Wu, Chenghao Liu, Xiaoli Li, and Jie Zheng. S1<sup>2</sup>mf: Predicting synthetic lethality in human cancers via logistic matrix factorization. *IEEE ACM Trans. Comput. Biol. Bioinform.*, 17(3):748–757, 2020.
  24. Herty Liany, Anand Jeyasekharan, and Vaibhav Rajan. Predicting synthetic lethal interactions using heterogeneous data sources. *Bioinform.*, 36(7):2209–2216, 2020.
  25. Jiang Huang, Min Wu, Fan Lu, Le Ou-Yang, and Zexuan Zhu. Predicting synthetic lethal interactions in human cancers using graph regularized self-representative matrix factorization. *BMC Bioinform.*, 20-S(19):657, 2019.
  26. Wout Megchelenbrink, Rotem Katzir, Xiaowen Lu, Eytan Ruppin, and Richard A Notebaart. Synthetic dosage lethality in the human metabolic network is highly predictive of tumor growth and cancer patient survival. *PNAS*, 2015.
  27. Angel A Ku, Hsien-Ming Hu, Xin Zhao, Khyati N Shah, Sameera Kongara, Di Wu, Frank McCormick, Allan Balmain, and Sourav Bandyopadhyay. Integration of multiple biological contexts reveals principles of synthetic lethality that affect reproducibility. *Nature communications*, 11(1):2375, 2020.
  28. Naroa Barrena, Luis V Valcárcel, Danel Olaverri-Mendizabal, Iñigo Apaolaza, and Francisco J Planes. Synthetic lethality in large-scale integrated metabolic and regulatory network models of human cells. *npj Systems Biology and Applications*, 9(1):32, 2023.
  29. Sri R Paladugu, Shan Zhao, Animesh Ray, and Alpan Raval. Mining protein networks for synthetic genetic interactions. *Bmc Bioinformatics*, 9:1–14, 2008.
  30. JiaRui Li, Lin Lu, Yu-Hang Zhang, Min Liu, Lei Chen, Tao Huang, and Yu-Dong Cai. Identification of synthetic lethality based on a functional network by using machine learning algorithms. *Journal of cellular biochemistry*, 120(1):405–416, 2019.
  31. Yuyang Dou, Yujie Ren, Xinmiao Zhao, Jiaming Jin, Shizheng Xiong, Lulu Luo, Xinru Xu, Xueni Yang, Jiafeng Yu, Li Guo, et al. Csslbd: Discovery of cancer-specific synthetic lethal interactions based on machine learning and statistic inference. *Computers in Biology and Medicine*, 170:108066, 2024.
  32. Ruichu Cai, Xuexin Chen, Yuan Fang, Min Wu, Yuexing Hao, and Jonathan D. Wren. Dual-dropout graph convolutional network for predicting synthetic lethality in human cancers. *Bioinform.*, 36(16):4458–4465, 2020.
  33. Xinguo Lu, Guanyuan Chen, Jinxin Li, Xiangjin Hu, and Fengxu Sun. Magcn: A multiple attention graph convolution networks for predicting synthetic lethality. *IEEE/ACM Transactions on Computational Biology and Bioinformatics*, 20(5):2681–2689, 2023.
  34. Mincai Lai, Guangyao Chen, Haochen Yang, Jingkang Yang, Zhihao Jiang, Min Wu, and Jie Zheng. Predicting synthetic lethality in human cancers via multi-graph

- ensemble neural network. In *2021 43rd Annual International Conference of the IEEE Engineering in Medicine & Biology Society*.
35. Yahui Long, Min Wu, Yong Liu, Jie Zheng, Chee Keong Kwoh, Jiawei Luo, and Xiaoli Li. Graph contextualized attention network for predicting synthetic lethality in human cancers. *Bioinform.*, 37(16):2432–2440, 2021.
  36. Zhifeng Hao, Di Wu, Yuan Fang, Min Wu, Ruichu Cai, and Xiaoli Li. Prediction of synthetic lethal interactions in human cancers using multi-view graph auto-encoder. *IEEE J. Biomed. Health Informatics*, 25(10):4041–4051, 2021.
  37. Yahui Long, Min Wu, Yong Liu, Yuan Fang, Chee Keong Kwoh, Jimiao Chen, Jiawei Luo, and Xiaoli Li. Pre-training graph neural networks for link prediction in biomedical networks. *Bioinform.*, 38(8):2254–2262, 2022.
  38. Shike Wang, Yimiao Feng, Xin Liu, Yong Liu, Min Wu, and Jie Zheng. Nsf4sl: negative-sample-free contrastive learning for ranking synthetic lethal partner genes in human cancers. *Bioinformatics*, 38(Supplement\_2):ii13–ii19, 2022.
  39. Ge Zhang, Yitong Chen, Chaokun Yan, Jianlin Wang, Wenjuan Liang, Junwei Luo, and Huimin Luo. Mpsal: multi-perspective learning knowledge graph attention network for synthetic lethality prediction in human cancer. *Frontiers in Pharmacology*, 15:1398231, 2024.
  40. Ke Zhang, Yimiao Feng, and Jie Zheng. Prompt-based generation of natural language explanations of synthetic lethality for cancer drug discovery. In *LREC-COLING 2024*, pages 13131–13142, 2024.
  41. Kunjie Fan, Shan Tang, Birkan Gökbağ, Lijun Cheng, and Lang Li. Multi-view graph convolutional network for cancer cell-specific synthetic lethality prediction. *Frontiers in Genetics*, 13:1103092, 2023.
  42. Naftali Tishby, Fernando C. N. Pereira, and William Bialek. The information bottleneck method. *CoRR*, physics/0004057, 2000.
  43. Qingyun Sun, Jianxin Li, Hao Peng, Jia Wu, Xingcheng Fu, Cheng Ji, and Philip S. Yu. Graph structure learning with variational information bottleneck. In *AAAI 2022*.
  44. Yonglong Tian, Chen Sun, Ben Poole, Dilip Krishnan, Cordelia Schmid, and Phillip Isola. What makes for good views for contrastive learning? *NeurIPS 2020*.
  45. Xiang Wang, Xiangnan He, Yixin Cao, Meng Liu, and Tat-Seng Chua. Kgat: Knowledge graph attention network for recommendation. In *KDD*, 2019.
  46. Eric Jang, Shixiang Gu, and Ben Poole. Categorical reparameterization with gumbel-softmax. In *ICLR 2017*.
  47. Keyulu Xu, Weihua Hu, Jure Leskovec, and Stefanie Jegelka. How powerful are graph neural networks? In *ICLR 2019*.
  48. Haggai Maron, Heli Ben-Hamu, Hadar Serviansky, and Yaron Lipman. Provably powerful graph networks. *NeurIPS 2019*.
  49. Yimiao Feng, Yahui Long, He Wang, Yang Ouyang, Quan Li, Min Wu, and Jie Zheng. Benchmarking machine learning methods for synthetic lethality prediction in cancer. *Nature Communications*, 15:9058, 2024.
  50. Jie Wang, Min Wu, Xuhui Huang, Li Wang, Sophia Zhang, Hui Liu, and Jie Zheng. Synlethdb 2.0: a web-based knowledge graph database on synthetic lethality for novel anticancer drug discovery. *Database*, 2022:baac030, 2022.
  51. Eui-Hwan Choi and Keun Pil Kim. E2f1 facilitates dna break repair by localizing to break sites and enhancing the expression of homologous recombination factors. *Experimental & molecular medicine*, 51(9), 2019.
  52. Chih-Kuan Yeh, Cheng-Yu Hsieh, Arun Suggala, David I Inouye, and Pradeep K Ravikumar. On the (in) fidelity and sensitivity of explanations. *Advances in neural information processing systems*, 32, 2019.
  53. Prasad Chalasani, Jiefeng Chen, Amrita Roy Chowdhury, Xi Wu, and Somesh Jha. Concise explanations of neural networks using adversarial training. In *International Conference on Machine Learning*, pages 1383–1391. PMLR, 2020.
  54. Emanuel Parzen. On estimation of a probability density function and mode. *ANN*, 33(3), 1962.
  55. Mukund Sundararajan, Ankur Taly, and Qiqi Yan. Axiomatic attribution for deep networks. In *International conference on machine learning*, pages 3319–3328. PMLR, 2017.
  56. Zhitao Ying, Dylan Bourgeois, Jiaxuan You, Marinka Zitnik, and Jure Leskovec. Gnnexplainer: Generating explanations for graph neural networks. *Advances in neural information processing systems*, 32, 2019.
  57. Dongsheng Luo, Wei Cheng, Dongkuan Xu, Wenchao Yu, Bo Zong, Haifeng Chen, and Xiang Zhang. Parameterized explainer for graph neural network. *NeurIPS 2020*.
  58. Qiang Huang, Makoto Yamada, Yuan Tian, Dinesh Singh, and Yi Chang. Graphlime: Local interpretable model explanations for graph neural networks. *IEEE Trans. Knowl. Data Eng.*, 35(7):6968–6972, 2023.
  59. Jingyu Peng, Qi Liu, Linan Yue, Zaixi Zhang, Kai Zhang, and Yunhao Sha. Towards few-shot self-explaining graph neural networks. volume 14946 of *Lecture Notes in Computer Science*, pages 109–126. Springer, 2024.
  60. Antonio Longa, Steve Azzolin, Gabriele Santin, Giulia Cencetti, Pietro Liò, Bruno Lepri, and Andrea Passerini. Explaining the explainers in graph neural networks: a comparative study. *ACM Computing Surveys*, 2024.
  61. Junchi Yu, Jie Cao, and Ran He. Improving subgraph recognition with variational graph information bottleneck. In *Proceedings of the IEEE/CVF Conference on Computer Vision and Pattern Recognition*, pages 19396–19405, 2022.
  62. Sangwoo Seo, Sungwon Kim, and Chanyoung Park. Interpretable prototype-based graph information bottleneck. *NeurIPS 2024*.
  63. Zaixi Zhang, Qi Liu, Hao Wang, Chengqiang Lu, and Cheekong Lee. Protgnn: Towards self-explaining graph neural networks. In *Proceedings of the AAAI Conference on Artificial Intelligence*, volume 36, pages 9127–9135, 2022.
  64. Yingxin Wu, Xiang Wang, An Zhang, Xiangnan He, and Tat-Seng Chua. Discovering invariant rationales for graph neural networks. In *The Tenth International Conference on Learning Representations, ICLR 2022, Virtual Event, April 25-29, 2022*, 2022.
  65. Gang Liu, Tong Zhao, Jiaxin Xu, Tengfei Luo, and Meng Jiang. Graph rationalization with environment-based augmentations. In *Proceedings of the 28th ACM SIGKDD Conference on Knowledge Discovery and Data Mining*, pages 1069–1078, 2022.
  66. Mincai Lai, Guangyao Chen, Haochen Yang, Jingkang Yang, Zhihao Jiang, Min Wu, and Jie Zheng. Predicting synthetic lethality in human cancers via multi-graph ensemble neural network. In *43rd Annual International Conference of the IEEE Engineering in Medicine & Biology Society*. IEEE, 2021.

**Table 4.** Notations and Descriptions.

Notations	Descriptions
$(T)_{ij}, (T)_i$	Element at the $i$ -th row and the $j$ -th column of matrix $T$ , and the $i$ -th row of $T$ .
$G=(A, X, E)$	Joint graph data of the SL graph and KG.
$A, X, E$	Adjacency matrix, node feature matrix, and edge feature matrix of $G$ .
$G^{uv}=(A^{uv}, X^{uv}, E^{uv})$	Enclosing graph data for genes $u$ and $v$ .
$Y$	Binary SL interaction label of the gene pair $(u, v)$ .
$K \geq 1$	Number of explanations generated by DGIB4SL for a gene pair.
$d_0, d_1, d_2, d_3$	Dimensions of input features for nodes and relationships, relational space, and graph representation.
$\tilde{G}_k^{uv}=(\tilde{A}_k^{uv}, \tilde{X}_k^{uv})$	$k$ -th IB-graph data of $G^{uv}$ .
$\tilde{Z}_k^{uv} \in \mathbb{R}^{d_3}$	Graph representation of $\tilde{G}_k^{uv}$ .
$f_\phi^\mu(\tilde{Z}_k^{uv}), f_\phi^\Sigma(\tilde{Z}_k^{uv})$	Mean vector and diagonal covariance matrix of the distribution of $\tilde{Z}_k^{uv}$ .
$L^{uv} \in \mathbb{R}^{K \times K}$	Inner product of $K$ graph representations $\tilde{Z}_1^{uv}, \dots, \tilde{Z}_K^{uv}$ .
$B_k^{uv}$	Learnable edge importance weight matrix of $\tilde{G}_k^{uv}$ .
$\beta_1, \beta_2$	Coefficients of KL and DPP in the DGIB objective function.
$\Omega_i, M_i^{uv}$	Motif-based adjacency matrix of $\tilde{G}^{uv}$ for a given motif $\Omega_i$ .
$W_k^1, W_k^2, \theta, \phi$	Learnable parameters.

67. Antoine Bordes, Nicolas Usunier, Alberto García-Durán, Jason Weston, and Oksana Yakhnenko. Translating embeddings for modeling multi-relational data. In *Advances in 27th Annual Conference on Neural Information Processing Systems 2013*.
68. Lawrence Page, Sergey Brin, Rajeev Motwani, and Terry Winograd. The pagerank citation ranking: Bringing order to the web. Technical Report 1999-66, Stanford InfoLab, November 1999.

## Appendix

### Explainability in graph neural networks

As GNNs are increasingly applied to SL prediction, understanding the reasoning behind their predictions becomes critical. The explainability of GNNs can be broadly categorized into two classes: post-hoc explanations and self-explainable GNNs. Post-hoc methods build an additional explainer to interpret a trained GNN, using techniques such as gradients [55], perturbation [56, 57], or interpretable linear agents [58]. However, these methods often fail to reveal the true reasoning process due to the inherent non-convexity and complexity of GNNs [59, 60]. Self-explainable GNNs address the limitations of post-hoc approaches by providing predictions and explanations simultaneously. Two major directions in this area are: (1) Information bottleneck (IB) approaches: these methods use the IB principle [42] as a training objective to extract subgraphs closely related to graph labels [14, 13, 61, 62]. (2) Prototype learning: approaches like ProtGNN [63] identify subgraphs most relevant to graph patterns associated with specific classes. Beyond these, other methods like DIR [64] identifies causal patterns via distribution interventions and models classifiers based on causal and non-causal components, while GREA [65] introduces environment replacement to generate virtual data examples for better pattern identification. Despite their advantages, these methods face challenges when applied to SL prediction. Similar to KG-based approaches, self-explainable GNNs are limited in generating multiple explanations and capturing higher-order graph structures essential for prediction.

### Intuition for Measuring Diversity in Eq. 3

Intuitively, each entry in the matrix  $L^{uv}$  in Eq. 4 represents the similarity between the representations of two elements in the set, computed using dot products. Eq. 3 measures the diversity of elements within a set by leveraging the principle that, when the feature vectors of the elements are not linearly correlated, the volume of the hypercube they form is maximized. Consequently, the determinant of  $L^{uv}$  in Eq. 3 quantifies this volume, effectively capturing the diversity of the feature vectors [16].

### Proof of Eq. 6

**Proposition 1** (*Upper bound of  $-I(Y; \tilde{G}_k^{uv})$* ). For a graph  $G^{uv}$  with label  $Y$  and the  $k$ -th IB-Graph  $\tilde{G}_k^{uv}$  learned from  $G^{uv}$ , we have

$$-I(Y; \tilde{G}_k^{uv}) \leq -\mathbb{E}_{Y, \tilde{G}_k^{uv}} \left[ \log q_\theta(Y | \tilde{G}_k^{uv}) \right] + H(Y), \quad (16)$$

where  $q_\theta(Y | \tilde{G}_k^{uv})$  parameterized by  $\theta$  is the variational approximation of  $p(Y | \tilde{G}_k^{uv})$ .

*Proof*

$$\begin{aligned} I(Y; \tilde{G}_k^{uv}) &= \int \int p(Y, \tilde{G}_k^{uv}) \log \frac{p(Y, \tilde{G}_k^{uv})}{p(Y)p(\tilde{G}_k^{uv})} dY d\tilde{G}_k^{uv} \\ &= \int \int p(Y, \tilde{G}_k^{uv}) \log \frac{p(Y | \tilde{G}_k^{uv})}{p(Y)} dY d\tilde{G}_k^{uv} \\ &= \mathbb{E}_{Y, \tilde{G}_k^{uv}} \left[ \log \frac{p(Y | \tilde{G}_k^{uv})}{p(Y)} \right] \end{aligned} \quad (17)$$

Since  $p(Y | \tilde{G}_k^{uv})$  is intractable, we introduce a variational approximation  $q_\theta(Y | \tilde{G}_k^{uv})$  for it. Then we have

$$\begin{aligned} I(Y; \tilde{G}_k^{uv}) &= \mathbb{E}_{Y, \tilde{G}_k^{uv}} \left[ \log \frac{q_\theta(Y | \tilde{G}_k^{uv})}{p(Y)} \frac{p(Y | \tilde{G}_k^{uv})}{q_\theta(Y | \tilde{G}_k^{uv})} \right] \\ &= \mathbb{E}_{Y, \tilde{G}_k^{uv}} \left[ \log \frac{q_\theta(Y | \tilde{G}_k^{uv})}{p(Y)} \right] + \mathbb{E}_{Y, \tilde{G}_k^{uv}} \left[ \log \frac{p(Y | \tilde{G}_k^{uv})}{q_\theta(Y | \tilde{G}_k^{uv})} \right], \end{aligned} \quad (18)$$

where

$$\begin{aligned}
 & \mathbb{E}_{Y, \tilde{G}_k^{uv}} \left[ \log \frac{p(Y|\tilde{G}_k^{uv})}{q_\theta(Y|\tilde{G}_k^{uv})} \right] \\
 &= \int \int p(\tilde{G}_k^{uv}) p(Y|\tilde{G}_k^{uv}) \log \frac{p(Y|\tilde{G}_k^{uv})}{q_\theta(Y|\tilde{G}_k^{uv})} dY d\tilde{G}_k^{uv} \quad (19) \\
 &= \mathbb{E}_{\tilde{G}_k^{uv}} [D_{KL}(p(Y|\tilde{G}_k^{uv})||q_\theta(Y|\tilde{G}_k^{uv}))].
 \end{aligned}$$

Plug Eq. 19 into Eq. 18, we have

$$\begin{aligned}
 & I(Y; \tilde{G}_k^{uv}) \\
 &= \mathbb{E}_{Y, \tilde{G}_k^{uv}} \left[ \log \frac{q_\theta(Y|\tilde{G}_k^{uv})}{p(Y)} \right] + \mathbb{E}_{\tilde{G}_k^{uv}} [D_{KL}(p(Y|\tilde{G}_k^{uv})||q_\theta(Y|\tilde{G}_k^{uv}))] \\
 &\geq \mathbb{E}_{Y, \tilde{G}_k^{uv}} \left[ \log \frac{q_\theta(Y|\tilde{G}_k^{uv})}{p(Y)} \right] \quad (\text{non-negativity of KL Divergence}) \\
 &= \mathbb{E}_{Y, \tilde{G}_k^{uv}} \left[ \log q_\theta(Y|\tilde{G}_k^{uv}) \right] - \mathbb{E}_{Y, \tilde{G}_k^{uv}} [\log p(Y)] \\
 &= \mathbb{E}_{Y, \tilde{G}_k^{uv}} \left[ \log q_\theta(Y|\tilde{G}_k^{uv}) \right] - H(Y) \quad (\text{normalization of} \\
 &\quad \text{PDF } p(\tilde{G}_k^{uv}|Y)) \\
 &\Rightarrow -I(Y; \tilde{G}_k^{uv}) \leq -\mathbb{E}_{Y, \tilde{G}_k^{uv}} \left[ \log q_\theta(Y|\tilde{G}_k^{uv}) \right] + H(Y) \quad (20)
 \end{aligned}$$

where  $H(Y)$  is the entropy of label  $Y$ , which can be ignored in the optimization procedure.  $\square$

**Proposition 2 (Upper bound of  $I(G^{uv}; \tilde{G}_k^{uv})$ ).** For a graph  $G^{uv}$  and the  $k$ -th IB-Graph  $\tilde{G}_k^{uv}$  learned from  $G^{uv}$ , we have

$$I(G^{uv}; \tilde{G}_k^{uv}) \leq \mathbb{E}_{G^{uv}} [D_{KL}(q_\phi(\tilde{G}_k^{uv}|G^{uv})||q(\tilde{G}_k^{uv}))], \quad (21)$$

where  $q(\tilde{G}_k^{uv}) = \sum_{G^{uv}} p(G^{uv}) q_\phi(\tilde{G}_k^{uv}|G^{uv})$  and  $q_\phi(\tilde{G}_k^{uv}|G^{uv})$  parameterized by  $\phi$  is the variational approximation of  $p(\tilde{G}_k^{uv}|G^{uv})$ ,  $D_{KL}(\cdot)$  denotes the Kullback-Leibler (KL) divergence.

*Proof*

$$\begin{aligned}
 I(G^{uv}; \tilde{G}_k^{uv}) &= \int \int p(G^{uv}, \tilde{G}_k^{uv}) \log \frac{p(G^{uv}, \tilde{G}_k^{uv})}{p(G^{uv})p(\tilde{G}_k^{uv})} dG^{uv} d\tilde{G}_k^{uv} \\
 &= \int \int p(G^{uv}, \tilde{G}_k^{uv}) \log \frac{q_\phi(\tilde{G}_k^{uv}|G^{uv})}{p(\tilde{G}_k^{uv})} dG^{uv} d\tilde{G}_k^{uv} \\
 &= \mathbb{E}_{G^{uv}, \tilde{G}_k^{uv}} \left[ \log \frac{q_\phi(\tilde{G}_k^{uv}|G^{uv})}{p(\tilde{G}_k^{uv})} \right]. \quad (22)
 \end{aligned}$$

Since  $p(\tilde{G}_k^{uv})$  is intractable, we introduce a variational approximation  $q(\tilde{G}_k^{uv}) = \sum_{G^{uv}} p(G^{uv}) q_\phi(\tilde{G}_k^{uv}|G^{uv})$  for the marginal distribution  $p(\tilde{G}_k^{uv})$ . Then we have

$$\begin{aligned}
 I(G^{uv}; \tilde{G}_k^{uv}) &= \mathbb{E}_{G^{uv}, \tilde{G}_k^{uv}} \left[ \log \frac{q(\tilde{G}_k^{uv}) q_\phi(\tilde{G}_k^{uv}|G^{uv})}{p(\tilde{G}_k^{uv}) q(\tilde{G}_k^{uv})} \right] \\
 &= \mathbb{E}_{G^{uv}, \tilde{G}_k^{uv}} \left[ \log \frac{q_\phi(\tilde{G}_k^{uv}|G^{uv})}{q(\tilde{G}_k^{uv})} \right] + \mathbb{E}_{G^{uv}, \tilde{G}_k^{uv}} \left[ \log \frac{q(\tilde{G}_k^{uv})}{p(\tilde{G}_k^{uv})} \right] \quad (23) \\
 &= \mathbb{E}_{G^{uv}, \tilde{G}_k^{uv}} \left[ \log \frac{q_\phi(\tilde{G}_k^{uv}|G^{uv})}{q(\tilde{G}_k^{uv})} \right] - \mathbb{E}_{G^{uv}, \tilde{G}_k^{uv}} \left[ \log \frac{p(\tilde{G}_k^{uv})}{q(\tilde{G}_k^{uv})} \right],
 \end{aligned}$$

where

$$\begin{aligned}
 & \mathbb{E}_{G^{uv}, \tilde{G}_k^{uv}} \left[ \log \frac{p(\tilde{G}_k^{uv})}{q(\tilde{G}_k^{uv})} \right] \\
 &= \int p(\tilde{G}_k^{uv}) \log \frac{p(\tilde{G}_k^{uv})}{q(\tilde{G}_k^{uv})} \int p(G^{uv}|\tilde{G}_k^{uv}) dG^{uv} d\tilde{G}_k^{uv} \quad (24) \\
 &= \int p(\tilde{G}_k^{uv}) \log \frac{p(\tilde{G}_k^{uv})}{q(\tilde{G}_k^{uv})} d\tilde{G}_k^{uv} \\
 &= D_{KL}(p(\tilde{G}_k^{uv})||q(\tilde{G}_k^{uv}))
 \end{aligned}$$

Plug Eq. 24 into Eq. 23, we have

$$\begin{aligned}
 I(G^{uv}; \tilde{G}_k^{uv}) &= \mathbb{E}_{G^{uv}, \tilde{G}_k^{uv}} \left[ \log \frac{q_\phi(\tilde{G}_k^{uv}|G^{uv})}{q(\tilde{G}_k^{uv})} \right] - D_{KL}(p(\tilde{G}_k^{uv})||q(\tilde{G}_k^{uv})) \\
 &\leq \mathbb{E}_{G^{uv}, \tilde{G}_k^{uv}} \left[ \log \frac{q_\phi(\tilde{G}_k^{uv}|G^{uv})}{q(\tilde{G}_k^{uv})} \right] \quad (\text{non-negativity of KL Divergence}) \\
 &= \mathbb{E}_{G^{uv}} [D_{KL}(q_\phi(\tilde{G}_k^{uv}|G^{uv})||q(\tilde{G}_k^{uv}))] \quad (25) \\
 &\quad \square
 \end{aligned}$$

The calculation method of  $B_k^{uv}$

The calculation of  $B_k^{uv}$  is as follows: For any edge  $(i, j)$  not present in the enclosing graph  $G^{uv}$ ,  $(B_k^{uv})_{i,j}$  is fixed to 0, since our goal is to extract a subgraph from  $G^{uv}$ . For edges  $(i, j)$  in  $G^{uv} = (A^{uv}, X^{uv}, E^{uv})$ , inspired by the approaches of Wang et al. [45], we optimize  $(B_k^{uv})_{i,j}$  jointly with relational graph learning by the following function (corresponding to  $\psi_k$  in Fig. 2):

$$(B_k^{uv})_{i,j} := (W_k^1(X^{uv})_j) \cdot \tanh(W_k^1(X^{uv})_i + W_k^2(E^{uv})_r)^T, \quad (26)$$

where  $W_k^1 \in \mathbb{R}^{d_2 \times d_0}$  and  $W_k^2 \in \mathbb{R}^{d_2 \times d_1}$  are learnable weight matrices for mapping node and relation features into the same space, respectively. Here,  $(E^{uv})_r \in \mathbb{R}^{d_1}$  represents the feature of relation  $r$  in the triple  $(i, r, j)$  and  $\tanh(\cdot)$  is a nonlinear activation function. This formulation ensures that  $(B_k^{uv})_{i,j}$  depends on the distance between the features  $(X^{uv})_i$ ,  $(X^{uv})_j$  of nodes  $i$  and  $j$  in the space defined by relation  $r$  [45]. Intuitively,  $(B_k^{uv})_{i,j}$  reflects the SL prediction-specific importance of the edge, with smaller values indicating noise that should be assigned lower weights or excluded. Note that  $\tilde{A}_k^{uv}$  is not differentiable with respect to  $B_k^{uv}$  due to Bernoulli sampling, we employ the concrete relaxation [46] to approximate sampling for the IB-Graph:

$$(\tilde{A}_k^{uv})_{i,j} = \text{sigmoid}\left(\frac{1}{\tau} \left( \log \frac{(B_k^{uv})_{i,j}}{1 - (B_k^{uv})_{i,j}} + \log \frac{\epsilon}{1 - \epsilon} \right)\right), \quad (27)$$

where  $\epsilon \sim \text{Uniform}(0, 1)$  and  $\tau \in \mathbb{R}^+$  is the temperature of the concrete distribution.

## Construction of the IB-Graph

The construction process of the IB-Graph, as shown in Fig. 9, involves four steps, which slightly differ between the training and testing phases. During the training phase:

1. **Input:** The enclosing graph data  $G = (A, X, E)$  (with the superscript  $uv$  omitted for simplicity) is provided for a given gene pair  $(u, v)$ .

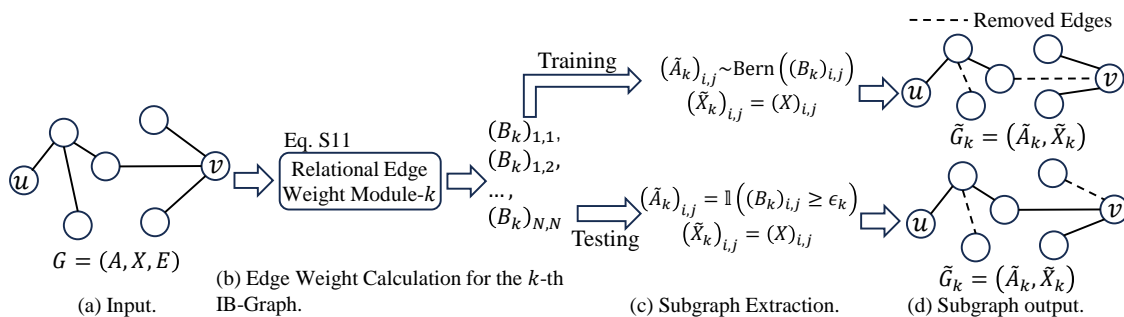


**Fig. 9.** Overview for extracting the  $k$ -th IB-graph from the enclosing graph  $G=(A, X, E)$  (for simplicity, the superscript  $uv$  is omitted) around the pair of genes  $u$  and  $v$ .

- Edge weight estimation:** The weights of all edges in  $G$  are estimated using Eq. 26, which serves as the edge-weighting module.
- Subgraph extraction:** These edge weights are treated as parameters of independent Bernoulli variables, and random sampling assigns each edge a value of 1 or 0.
- Subgraph output:** The sampled edge values are aggregated to form a binary adjacency matrix  $\tilde{A}_k$ , representing the adjacency matrix of the  $k$ -th IB-graph. The node feature matrix  $\tilde{X}_k$  is retained as equal to  $X$ , as our focus is on edge-level explanation.

Note that sampling from a Bernoulli distribution is not differentiable, the Gumbel-Softmax trick is thus used during optimization, as detailed in Eq. 27.

In the testing phase, the process differs only in the third step. Instead of sampling, a predefined importance threshold  $\epsilon_k$ , derived from the learned importance distribution, determines whether an edge exists. In our experiments, this threshold is set as the median of the ranked edge weights in  $B_k$ . The reason why the subgraph extraction methods in the third step differ is that subgraph selection during training is intended to optimize the model’s parameters, while during testing, it aims to infer the best estimation of the explanatory subgraph. This difference also aligns with the standard practice in GIB-based methods, as seen in the literature [14, 61].

## Detailed information of baselines

**Table 5.** Numbers of the entities in the SynLethKG.

Type	No. of entities
Gene	25,260
Biological process	12,703
Side effect	5,702
Molecular function	3,203
Pathway	2,069
Compound	2,065
Cellular component	1,670
Symptom	427
Anatomy	400
Pharmacologic class	377
Disease	136

We evaluated our DGIB4SL against two categories of methods: matrix factorization (MF)-based methods and graph

**Table 6.** Summary of the relationship in the SynLethKG.

Type	No. of entities
(Gene, Regulates, Gene)	267,791
(Gene, Interacts, Gene)	148,379
(Gene, Covaries, Gene)	62,987
(Anatomy, Expresses, Gene)	617,175
(Disease, Associates, Gene)	24,328
(Disease, Upregulates, Gene)	7,730
(Compound, Downregulates, Gene)	21,526
(Disease, Downregulates, Gene)	7,616
(Compound, Binds, Gene)	16,323
(Compound, Upregulates, Gene)	19,200
(Anatomy, Upregulates, Gene)	26
(Anatomy, Downregulates, Gene)	31
(Gene, Participates, Cellular component)	97,652
(Gene, Participates, Biological process)	619,712
(Compound, Causes, SideEffect)	139,428
(Gene, Participates, Molecular function)	110,042
(Gene, Participates, Pathway)	57,441
(Compound, Treats, Disease)	752
(Compound, Resembles, Compound)	6,266
(Pharmacologic Class, Includes, compound)	1,205
(Disease, Localizes, Anatomy)	3,373
(Disease, Presents, Symptom)	3,401
(Compound, Palliates, Disease)	384
(Disease, Resembles, Disease)	404

neural network (GNN)-based methods, selecting thirteen recent approaches.

- **GRSMF** [25] reconstructs the SL interaction graph using graph-regularized self-representative MF, incorporating PPI and GO for regularization.
- **SL<sup>2</sup>MF** [23] employs logistic MF for SL prediction, integrating importance weighting and PPI/GO information.

**Table 7.** Summary of the relationship in the core graphs in Fig. 4 output by DGIB4SL.

Label	Description
includes_PCiC	Pharmacological class includes compound.
palliates_Cpd	Compound palliates disease.
participates_GpMF	Gene participates in molecular function.
presents_Dps	Disease presents symptom.

- **CMFW** [24] combines multiple data sources using collective matrix factorization to generate latent representations.

GNN-based methods include:

- **DDGCN** [32] utilizes GCN with SL interaction matrix features and applies dropout techniques to address sparse graphs.
- **GCATSL** [35] uses a dual attention mechanism with SL, PPI, and GO as input graphs to complete the SL graph.
- **SLMGAE** [36] implements a multi-view graph autoencoder, integrating SL, PPI, and GO graphs for prediction.
- **MGE4SL** [66] leverages a Multi-Graph Ensemble to combine PPI, GO, and Pathway data using neural network embeddings.
- **PTGNN** [37] pre-trains GNNs with various data sources and graph-based reconstruction features.
- **KG4SL** [3] is the first GNN-based model to integrate a knowledge graph for SL prediction, utilizing an attention mechanism.
- **PiLSL** [4] extracts pairwise local subgraphs for SL prediction and integrates multi-omics data with attention mechanisms.
- **NSF4SL** [38] uses contrastive learning with pre-trained KG-based features (e.g., TransE[67]) as input for neural embeddings.
- **KR4SL** [5] encodes structural information, textual semantic information, and sequential semantics for gene representations, and uses different attention mechanisms to select important edges in each hop.
- **SLGNN** [6] generates gene embeddings with factor-based message passing and identifies important factors through attention mechanisms, where factors consist of relationships in the KG.

### Explainability evaluation metrics

Given the lack of ground-truth explanations in the SL dataset, we employed two metrics to evaluate explanation **accuracy**:

- **Infidelity** [52] measures explanation faithfulness, where more important features (e.g., edges or relational features) should cause larger prediction changes when altered. It introduces random perturbations to the input features, weights them by importance, and compares the changes in features and predictions to evaluate consistency.
- **Sparseness** [53] evaluates explanation sparsity using the Gini index. Higher Sparseness indicates that the explanation concentrates on fewer important features, effectively reducing redundant information.

### Implementation details

To evaluate the effectiveness of our DGIB4SL, we adopted the same data processing, splitting, and evaluation metrics as SLB [49]. For dataset processing, the number of positive samples (i.e. known SL pairs) was balanced with an equal number of negative samples. Negative samples were generated using a common strategy of randomly selecting gene pairs from unknown samples.

The configuration of DGIB4SL and baseline models for the SL prediction task was as follows: For our DGIB4SL, we set  $d_2=d_3=6$  (Eq. 26, Eq. 4). Next, the coefficients  $\beta_1$  and  $\beta_2$  in Eq. 6 were set  $\beta_1=\beta_2=10^{-4}$ . We further set the number

of explanations  $K$  in Eq. 6 for each sample to 3 (for the appropriate range of  $K$ , please refer to the next section). We used the Stochastic Gradient Descent (SGD) optimizer with a learning rate 0.005. The maximum number of training epochs was set as 5. For the baselines, we tuned their settings according to SLB [49]. Specifically, the output embedding dimension was set to 256 and the hidden embedding dimension was set to 512. The learning rate was tuned empirically. An early stopping strategy was used to avoid overfitting during training. The number of layers in most GNNs was set to 1, except for KR4SL, which used a 3-layer GNN to generate path-based explanations. We set the rank position  $C$  in the ranking metrics to 10 and 50 to represent 0.1% and 0.7% of the 7,183 candidate gene pairs, offering two levels of ranking difficulty. These values also align with those used in related studies (e.g., NSF4SL [38], KR4SL [5]).

### Determining the range of $K$

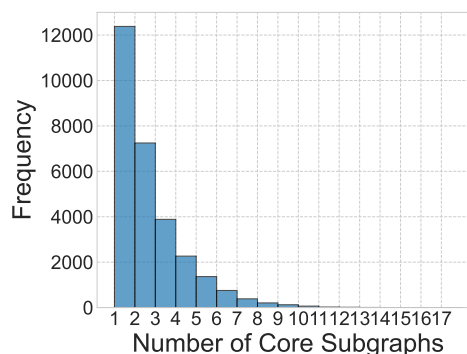


**Fig. 10.** Frequency histogram of estimated core subgraphs for SL pairs enclosing graphs in the training set.

To determine the range of  $K$  (the number of explanations generated by DGIB4SL for each gene pair), it is necessary to clearly specify its lower and upper bounds. The lower bound is the minimum number of core subgraphs across all SL gene pairs, which is clearly 1. The upper bound represents the maximum number of core subgraphs among all possible SL gene pairs. Since calculating the exact number of core subgraphs for all SL gene pairs is unrealistic, we use a heuristic approach to estimate the range of  $K$  based on the training set. This method is guided by the intuition that core subgraphs are densely connected internally and sparsely connected externally, which is divided into 4 steps:

1. For each SL gene pair in the training set, we compute node importance scores in the enclosing graph using the PageRank (PR) algorithm [68].
2. Nodes with importance scores below the 90-*th* percentile are considered unimportant and removed from the graph.
3. The number of connected components formed by the remaining nodes serves as an estimate of the number of core subgraphs in the given enclosing graph.
4. Fig. 10 presents the frequency histogram of core subgraph counts in the training set. Thus, the approximate range for  $K$  is [1, 17].